Mon. Not. R. Astron. Soc. **000**, 1–21 (2013) Printed 10 April 2014 (MN LATEX style file v2.2)

Re-growth of stellar disks in mature galaxies: The two component nature of NGC 7217 revisited with VIRUS-W †,◇

Maximilian H. Fabricius,[1,2⋆] Lodovico Coccato,[3,4] Ralf Bender,[1,2] Niv Drory,[5] Claus Gössl,[2] Martin Landriau,[5] Roberto P. Saglia,[1] Jens Thomas,[1] Michael J. Williams[1,6]

[1] *Max Planck Institute for Extraterrestrial Physics, Giessenbachstraße, 85748 Garching, Germany*
[2] *University Observatory Munich, Scheinerstraße 1, 81679 Munich, Germany*
[3] *European Southern Observatory, Karl-Schwarzschild-Straße 2, D-85748 Garching bei Muenchen, Germany*
[4] *ICG, University of Portsmouth, Dennis Sciama Building, Burnaby Road, Portsmouth, PO1 3FX, United Kingdom.*
[5] *McDonald Observatory, The University of Texas at Austin, 2515 Speedway, Stop C1402, Austin, Texas 78712-1206, USA*
[6] *Department of Astronomy, Columbia University, New York 10027, USA*

arXiv:1404.2272v1 [astro-ph.GA] 8 Apr 2014

10 April 2014

ABSTRACT

Previous studies have reported the existence of two counter-rotating stellar disks in the early-type spiral galaxy NGC 7217. We have obtained high-resolution optical spectroscopic data ($R \approx 9000$) with the new fiber-based Integral Field Unit instrument VIRUS-W at the 2.7 m telescope of the McDonald Observatory in Texas. Our analysis confirms the existence of two components. However, we find them to be co-rotating. The first component is the more luminous ($\approx 77\%$ of the total light), has the higher velocity dispersion ($\approx 170\,\mathrm{km\,s^{-1}}$) and rotates relatively slowly (projected $v_{\max} = 50\,\mathrm{km\,s^{-1}}$). The lower luminosity second component, ($\approx 23\%$ of the total light), has a low velocity dispersion ($\approx 20\,\mathrm{km\,s^{-1}}$) and rotates quickly (projected $v_{max} = 150\,\mathrm{km\,s^{-1}}$). The difference in the kinematics of the two stellar components allows us to perform a kinematic decomposition and to measure the strengths of their Mg and Fe Lick indices separately. The rotational velocities and dispersions of the less luminous and faster component are very similar to those of the interstellar gas as measured from the [O III] emission. Morphological evidence of active star formation in this component further suggests that NGC 7217 may be in the process of (re)growing a disk inside a more massive and higher dispersion stellar halo. The kinematically cold and regular structure of the gas disk in combination with the central almost dust-free morphology allows us to compare the dynamical mass inside of the central 500 pc with predictions from a stellar population analysis. We find agreement between the two if a Kroupa stellar initial mass function is assumed.

†This paper includes data taken at The McDonald Observatory of The University of Texas at Austin.
◇This paper contains data obtained at the Wendelstein Observatory of the Ludwig-Maximilians University Munich.

Key words: galaxies: bulges — galaxies: evolution — galaxies: formation — galaxies: structure

1 INTRODUCTION

Photometric studies have been decomposing galaxies into multiple stellar components for a long time now (e.g. de Vaucouleurs 1959). The technique has become common practice in the attempt to disentangle the formation histories of galaxies. The problem of a kinematic decomposition, i.e. the detection of genuinely separate components in the line-of-sight velocity distributions (LOSVDs) — especially in later type galaxies — places higher demands on the data quality,

⋆ E-mail:mxhf@mpe.mpg.de

© 2013 RAS

both in terms of spectral resolution and signal-to-noise ratio. Nevertheless, disk-like structures have been detected in elliptical galaxies (Bender 1988; Franx & Illingworth 1988; Davies & Birkinshaw 1988; Jedrzejewski & Schechter 1989; Scorza & Bender 1990, 1995) and spectroscopic surveys now provide statistics on the occurrence of kinematic subcomponents in early-type (Krajnović et al. 2011), S0s (Kuijken, Fisher & Merrifield 1996), and spiral galaxies (Pizzella et al. 2004).

We have constructed a new, high-spectral resolution Integral Field Unit spectrograph called VIRUS-W (Fabricius et al. 2008, 2012a), that is designed specifically to study the stellar LOSVDs of nearby disk galaxies. It offers a spectral resolution of $R \approx 9000$ ($\sigma_{inst} = 15\,\mathrm{km\,s^{-1}}$) in the optical which allows us to resolve the low velocity dispersions of a few tens of $\mathrm{km\,s^{-1}}$ typically found in disky systems, and to study the fine structure of the corresponding LOSVDs.

As a test case, we observed the early-type spiral galaxy NGC 7217. Its dynamical structure has been of particular interest because it hosts multiple rings. There are two star-forming rings with diameters of $63''$ and $156''$, and a third inner dust ring with a diameter of $21''$ (Buta et al. 1995, hereafter B95). This inner nuclear ring marks a significant change in morphology: the outer flocculent spiral disappears completely and gives away to a smooth central light distribution (Fisher & Drory 2008, see Fig. 1). The ring locations seemingly correspond to resonances (Verdes-Montenegro, Bosma & Athanassoula 1995) but NGC 7217 does not host any obvious, non-axisymmetric structure such as a stellar bar that could create corresponding resonances. Given its relative isolation (Karachentseva 1973) tidal effects caused by other galaxies can also be ruled out as a source of the resonances. However, B95 carried out an extensive photometric analysis of NGC 7217 and through a Fourier analysis find a weak perturbation to the axisymmetry which may be a faded bar.

Previous work has claimed that NGC 7217 hosts a large-scale counter-rotating stellar disk (Merrifield & Kuijken 1994; Sil'chenko & Afanasiev 2000; Fabricius et al. 2012b), a phenomenon that has been observed only in a handful of systems so far. The prototypical example of this class of systems is NGC 4550, where its bimodal LOSVD reveals that ≈50% of the stars are on retrograde orbits (Rubin, Graham & Kenney 1992; Rix et al. 1992; Emsellem et al. 2004). Only a few similar objects are known: Prada et al. (1996) claim that NGC 7331 has a counter-rotating bulge, and Zeilinger et al. (2001) describe stellar counter-rotation in NGC 3521. NGC 3593 hosts a counter-rotating component that dominates the light in the central regions (Bertola et al. 1996). Further examples include NGC 4138 (Jore, Broeils & Haynes 1996; Haynes et al. 2000) and counter-rotation caused by interaction in NGC 5719 (Vergani et al. 2007; Coccato et al. 2011b).

It was hypothesized that the counter-rotation in NGC 7217 may be the result of a minor merger event or the cold accretion of gas (Merrifield & Kuijken 1994; Pizzella et al. 2004). The observed ring structure (Lovelace, Jore & Haynes 1997) has been attributed to both the putative minor merger (Sil'chenko & Moiseev 2006) and instabilities created by counter-rotation.

In an attempt to disentangle the two counter-rotating disks and to probe our ability to detect and to study kinematic substructure in stellar systems, we obtained observations of the central region of NGC 7217, covering one of its two stellar rings (see Fig. 1). We recover non-parametric LOSVDs with the proper treatment of nebular emission. We do not confirm the existence of counter-rotation in this galaxy. Rather we find a sub-dominant, kinematically cold and rapidly rotating stellar disk embedded in a higher dispersion, co-rotating essentially spherical stellar halo.

In the next section we will briefly describe the characteristics of the new spectrograph that we use for this work. In Section 3, we will then describe the observations. In Section 4, we discuss the basic data reduction, the algorithm that we use for the recovery of the non-parametric LOSVDs, the kinematic decomposition, and the method of direct spectral decomposition that we use to derive abundances of the two stellar components. In Section 5, we present kinematic maps for the two stellar components and the ionized gas. We also present maps for the line strength determinations of the two individual components. In Section 6 we analyse the gas velocity field through a tilted ring model and in Section 7 we derive a central mass-to-light ratio from the gas rotation and compare this value to the prediction from a stellar population analysis. We discuss the implications of our findings in Section 8, and summarize in Section 9.

2 THE INSTRUMENT

The observations of NGC 7217 were carried out using the VIRUS-W Integral Field Unit (IFU) spectrograph at the 2.7 m Harlan J. Smith Telescope of the McDonald Observatory in Texas. Its design is based on the Mitchell Spectrograph (Hill et al. 2008, formerly VIRUS-P), which is the prototype for the HETDEX survey instrument (Hill et al. 2010). Its IFU consists of 267 optical fibers that are arranged in a dense pack scheme in a rectangular field of view. Each fiber has a diameter of $150\,\mu$m or $3.2''$ on sky. The total field of view covers $105''\times55''$ with a fill factor of 1/3, such that three dithered exposures are needed to cover the field completely. The IFU is attached to the bent Cassegrain port of the 2.7 m which delivers a beam of $f/8$ that is converted to $f/3.65$ by the Mitchell Spectrograph's focal reducer. An iris shutter and an exchangeable optical filter for order separation and stray light reduction are placed in front of the focal reducer. A 25 m long fiber bundle guides the light to the instrument that is mounted on an optical bench inside the telescope control room.

The collimator of VIRUS-W accepts $f/3.22$ which is slightly faster than the nominal $f/3.65$ with which the fibers are fed. This allows for slight focal ratio degradation in the fibers. Two Volume Phase Holographic gratings offer two modes of spectral resolution. The higher resolution kinematics mode used in this work covers the spectral range of 4850 Å–5480 Å with a resolution of $R \approx 8700$ ($\sigma_{\mathrm{inst}} = 15\,\mathrm{km\,s^{-1}}$) and a linear dispersion of $0.19\,\text{Å pixel}^{-1}$. We use a SDSS g-band filter in this mode.

The refractive camera of VIRUS-W is a significant deviation from the prototype design. It eliminates the central obscuration and increases the total efficiency of the instrument. Tests on standard stars have shown that, including atmosphere and telescope optics, the throughput peaks at 27%. A Marconi (today e2v) CCD44-82 back side illumi-

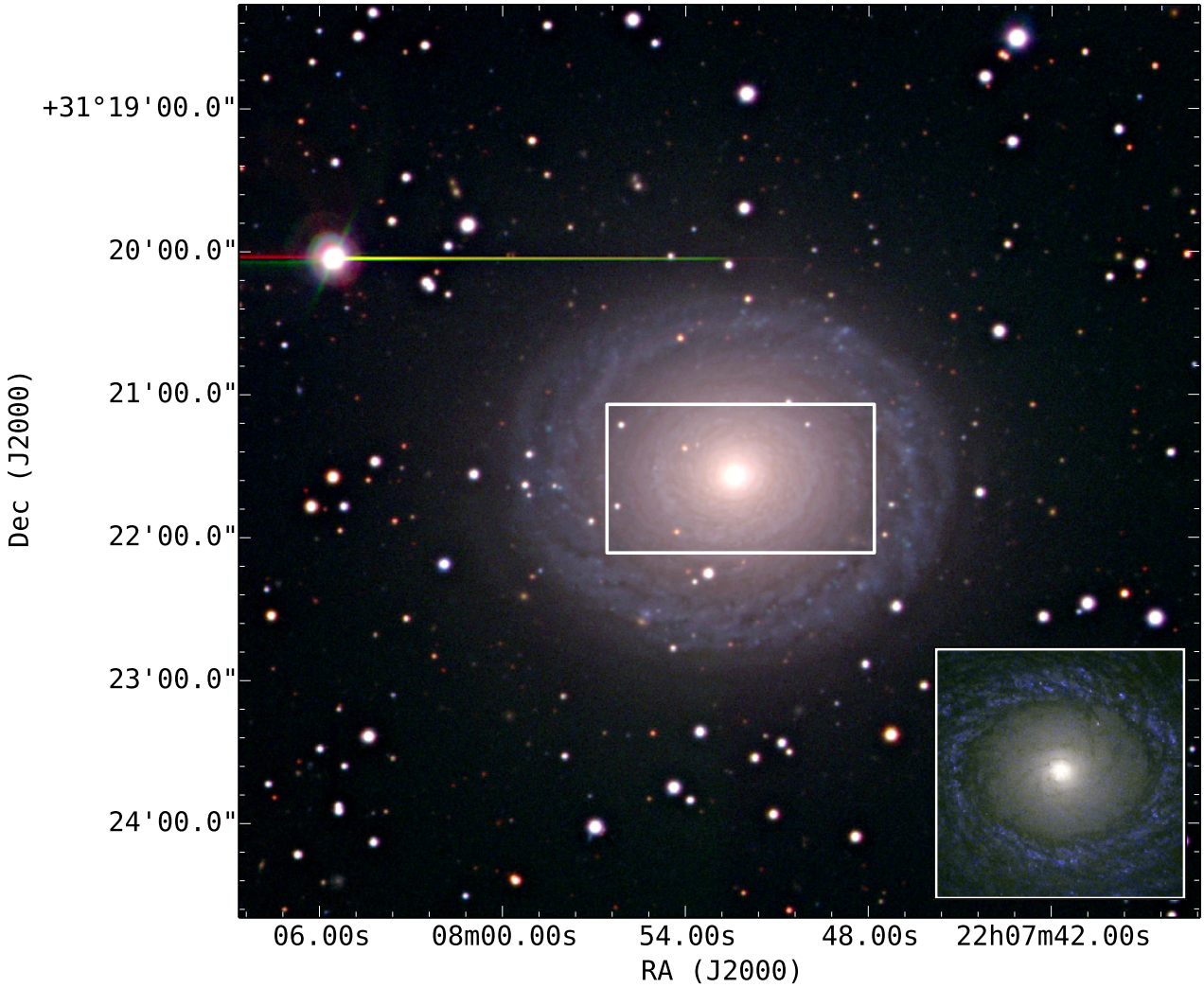

Figure 1. A *gri* composite of NGC 7217. The white box outlines $105'' \times 55''$ field of view of the VIRUS-W IFU. We obtained the images with the Wendelstein Wide Field Imager at the new 2 m Fraunhofer Telescope (Gössl et al. 2012; Hopp et al. 2012) on the 25 and the 27 of October 2013. The inset in the lower right shows an HST F450W/F336W false color composite of the central $25'' \times 25''$ (Program 11128; PI David Fisher).

nated 2k×4k 15 μm detector is used to record the spectra. At the operating temperature of $-130\,^{\circ}$C it has an average dark current of $4.1\,e^-$ pixel^{-1} h^{-1}. In the adopted science mode the camera electronics reads out at 100 kHz over two amplifiers with a gain of 1.61 ADU/e^- and a read noise of $2.55\,e^-$.

3 OBSERVATIONS

The observations were carried out in the nights of 2011 August 6, 7 and 9. We observed one field centered on the galaxy and dithered the observation by small offsets to fill the gaps between the fibers in the IFU. We obtained three 1800 s exposures in each dither position that we bracketed and interleaved with 600 s sky nods. The total on-object integration time per fiber is 1.5 h. The FWHM of the seeing varied between $1.0''$ and $1.3''$ during the observations. We took bias frames and simultaneous Hg and Ne arc lamp exposures for spectral calibration. We also recorded dome flats to trace the fiber positions on the detector and to compensate for fiber-to-fiber variation of the throughput.

Since the commissioning of VIRUS-W we have built up a library of spectra of stars to serve as kinematic template spectra (see Table 3) and to calibrate our data against the Lick system (Worthey et al. 1994).

4 DATA REDUCTION AND KINEMATIC EXTRACTION

4.1 Basic reduction

The basic data reduction is carried out using the `fitstools` package by (Gössl & Riffeser 2002). The generation of master bias, arc, and flat frames follows standard procedures. We use a slightly modified version of the Cure pipeline that was developed by our group for the HETDEX experiment (Hill et al. 2004) for the wavelength calibration and the spectral extraction. Cure first traces the fiber positions on the mas-

Table 1. Previously observed stellar templates.

Identifier	type	[Fe/H]	date of obs.	Flag
HR 2600	K2III	-0.35[1]	2010 Dec 02	K, S, L
HR 3369	G9III	0.16[1]	2010 Nov 15	K, S
HR 3418	K2III	0.11[1]	2010 Dec 02	K, S, L
HR 3427	K0III	0.16[1]	2010 Dec 02	K, S, L
HR 3428	K0III	0.23[2]	2010 Dec 03	K, S L
HR 3905	K0III	0.23[1]	2010 Dec 02	K, S, L
HR 4435	G9IV	-0.40[3]	2010 Dec 03	K, S, L
HR 6770	G8III	-0.05[1]	2010 Dec 03	K, S, L
HR 6817	K1III	-0.06[1]	2010 Dec 03	K, S, L
HR 7148	K1III	-0.09[1]	2011 May 26	K, S
HR 7176	K1III	0.17[1]	2011 May 27	K, S, L
HR 7576	K3III	0.42[1]	2010 Dec 04	K, S L
HR 8165	K1III	-0.09[1]	2011 May 25	K, S, L
HD 13791	G9III	—	2012 Feb 24	S
HD 64606	G8V	0.97[1]	2010 Dec 03	S
HD 74377	K3V	-0.07[1]	2010 Dec 03	S
HD 101501	G8V	-0.13[1]	2010 Dec 03	S, L
HD 107685	F6V	-0.06[3]	2012 Feb 24	S, L
HD 108154	F6	-0.06[3]	2012 Feb 24	S, L
HD 114762	F9V	-0.68[4]	2012 Feb 24	S, L
HD 161817	A2VI	-0.95[1]	2012 Feb 24	S, L

Notes: These stellar templates were previously observed with VIRUS-W, using the instrumental setup used for NGC 7217. Col. 1: Identifier. Col. 2: Spectral type. Col. 3: Metallicity: (1) from Sánchez-Blázquez et al. (2006), (2) from Koleva & Vazdekis (2012), (3) from Anderson & Francis (2012), and (4) from Árnadóttir, Feltzing & Lundström (2010). Col. 4: Date of Observation. Col. 5: Flag that specifies what we used the star for: K = used for kinematic measurement; S = used for spectroscopic decomposition; L = Lick spectrophotometric standard, used to compute the offset to the Lick system.

ters of the dome flat frames. It then extracts the positions of the spectral line peaks along these traces. The distortion and the spectral dispersion are modelled by a two-dimensional 7th degree Chebyshev polynomial. The corresponding model translates between pixel positions on the detector and fiber-wavelength pairs. Cure also calculates corresponding inverse and cross transformations.

We use 24 lines for the wavelength calibration. The standard deviation of fitted line positions to the model prediction is 0.1 pixel or 0.02 Å or $1.2\,\mathrm{km\,s^{-1}}$.

With the models in place, Cure extracts spectra from the science frames by *walking* along the previously determined trace positions. We use an extraction aperture that is 7 pixels wide. Tests have shown that this results in less than 1 % aperture loss and less than 0.1 % crosstalk between neighbouring spectra of equal signal level. The extraction is directly carried out in $\ln(\lambda)$-space with a spectral step width of $10\,\mathrm{km\,s^{-1}}$, which closely matches the physical pixel size of the detector. The signal is distributed in a flux-conserving manner from detector pixels to spectral elements according to two-dimensional overlap in area. The dome flat spectra are extracted in the same way as the science data.

The final reduction steps are carried out using a dedicated pipeline. At each wavelength we divide the signal of all fibers in the flat frames by their average signal at that wavelength. The resulting frame is used to correct the science and the sky frames for differences in the fiber-to-fiber transmission, vignetting of the spectrograph camera at the ends of the spectral range, and sensitivity variations of the detector.

For each science exposure, we average the surrounding sky spectra while rejecting spurious events. In order to increase the signal-to-noise ratio we average the sky signal of 20 neighbouring fibers in a moving window approach while further rejecting outliers through kappa-sigma clipping. The sky is then scaled according to the exposure time and subtracted from the science data.

The three flat-fielded and sky-subtracted science frames for each dither position are then averaged while further rejecting outliers. Finally, we combine the per-fiber spectra into a common datacube. The astrometry of the IFU is tied to the guider images and the sky positions of the individual fiber apertures are derived in as described in (Adams et al. 2011). We create a pixel grid that covers the whole field of view and set the pixel size to $1.6'' \times 1.6''$. We assign fluxes from fibers to pixels by calculating the overlap between the individual fiber apertures and the spatial extent of each pixel. This is done for all wavelength steps of the extracted spectra and results in a three-dimensional datacube with the dimensions RA, dec and $\ln(\lambda)$.

4.2 Recovery of non-parametric LOSVDs

A number of algorithms exist today which extract line-of-sight stellar velocity distributions from galaxy spectra. The Fourier Correlation Method (FCQ) by Bender (1990) recovers full line-of-sight velocity distributions. It is relatively stable against mismatches of the observed stellar templates and the intrinsic galaxy spectrum due to the method of the deconvolution of the peak of the cross-correlation function of the galaxy and the template spectrum. However, as it operates in Fourier space, masking of spectral regions is problematic, and potential contamination by nebular emission lines has to be treated outside of FCQ (Saglia et al. 2010; Fabricius et al. 2012a). The Maximum Penalized Likelihood Method (MPL) by (Gebhardt et al. 2000) overcomes the template mismatch problem by simultaneously fitting a linear combination of a set of different stellar templates. The relative weights of the different templates enter the optimisation routine as additional free parameters.

Similarly, the more recent Penalized Pixel-Fitting (Cappellari & Emsellem 2004, pPXF) operates in pixel space and uses a set of multiple template spectra. GANDALF (Sarzi et al. 2006) extends pPXF to model nebular emission lines and to include them in the fitting of the stellar kinematics. The latter two methods extract parametric velocity distributions by means of modelling them by a Gauss-Hermite expansion (Gerhard 1993).

In the case of NGC 7217 we expected very non-Gaussian LOSVDs and considered an a priori parametric treatment problematic. We therefore implemented a new algorithm that is based on MPL and recovers a non-parametric LOSVD, but extends MPL to treat nebular emission. After the removal of the continuum, the modelling of the stellar kinematics operates completely analogously to MPL. A linear combination of all template spectra is convolved with a trial LOSVD. A standard least square fitting routine (MINPACK `lmdif`, Moré, Garbow & Hillstrom 1980) minimizes the residuals between the galaxy spectrum and the broad-

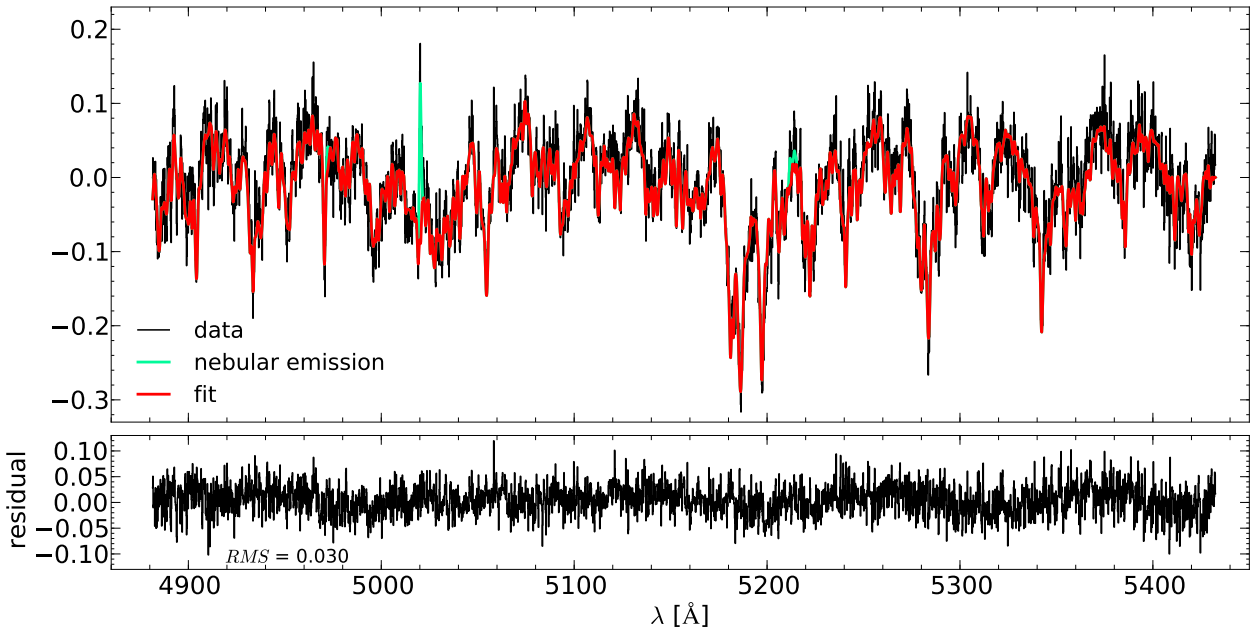

Figure 2. Example of a kinematic fit to bin 130. In the upper panel, we plot the actual recorded spectrum in black, the corresponding best-fitting stellar model spectrum in red, and the best-fitting gas model in green. The lower panel shows the residuals.

ened template by varying the amplitude of the individual velocity channels of the LOSVD and by adjusting the template weights. As in MPL we regularize by calculating the sum of the squared second derivative of the LOSVD. We then normalize the sum by dividing it by the number of velocity channels and multiply the result with a smoothing parameter before adding it to the residuals. A small smoothing factor will result in little regularisation and the fitted LOSVDs will tend to show noise-induced oscillations especially in their wings. If a large smoothing factor is chosen, then the routine is forced to produce a very smooth LOSVD at the cost of increasing the residuals. We chose a degree of regularisation that does not significantly affect the RMS of the difference between the observed and best-fitting model spectra. The statistical, relative variation of the RMS value is given by $1/\sqrt{2n}$, where n is the number of pixels in the spectrum. For our 3200-pixel spectra, the expected variation is 1.25%. We find that the use of a smoothing value of 5 never results in an increase of the RMS by more than 1% and use this value for the fit of all our spectra (see Appendix A).

Our fitted spectral range includes several emission lines. For an initial kinematic fit to the stellar continuum, the algorithm masks the regions of nebular emission based on the rest frame wavelength of the emission line, the systemic velocity and a predefined velocity range. The best-fitting model spectrum is then subtracted from the observed spectrum and the gas emission lines are fitted following a very similar methodology to GANDALF. Each emission line is modelled by a Gaussian with a central wavelength and a dispersion. The velocity and the dispersion are derived from a subset or a single bright line, while for the fainter lines only the amplitude is fitted.

In a second step, all parameters — i.e. all velocity channels of the LOSVD, all template weights and all parameters of the model for the gas emission — are refitted on the entire spectrum. The best fitting parameters from the first step are used as initial guesses. Both steps include one iteration of removal of spurious pixels through kappa-sigma clipping.

We use a Voronoi tessellation to bin our data using a Python version of the algorithm by Cappellari & Copin (2003) kindly provided by Eric Emsellem. We fit the spectral range from 4865 Å–5415 Å and model and remove the continuum with a 7th degree polynomial. We further use an initial set of 12 templates, including K and G giants with a range of different metallicities (see Table 3). We first fit a representative subset of all galaxy spectra and successively remove templates that are given very small weights from the list. Our final set contains four template spectra (HR 2600, HR 6770, HR 6817, and HR 7576). We fit 110 velocity channels and use a Gaussian with a velocity dispersion of 500km s^{-1} as initial guess for the LOSVD.

The fitted spectral range contains the [O III]λλ 4959,5007 Å and [N I]λλ 5198,5200 Å emission lines (see Fig. 2). All lines are included in the fit while the velocity and the dispersion are only derived from the brighter [O III] line at 5007 Å.

From the kinematic fit we obtain a median S/N of 30 per spectral pixel for all Voronoi bins. We determine errors to all parameters through the generation of 30 Monte Carlo realisations of synthetic spectra with artificial noise, based on the best fitting set of parameters for each spectrum.

4.3 Kinematic double-Gaussian decomposition

A visual inspection of the recovered LOSVDs immediately reveals a two-component nature (see Fig. 3): the majority of all distributions shows a narrow $\sigma \approx 20$ km s^{-1} peak that is superimposed on a significantly broader component. In a

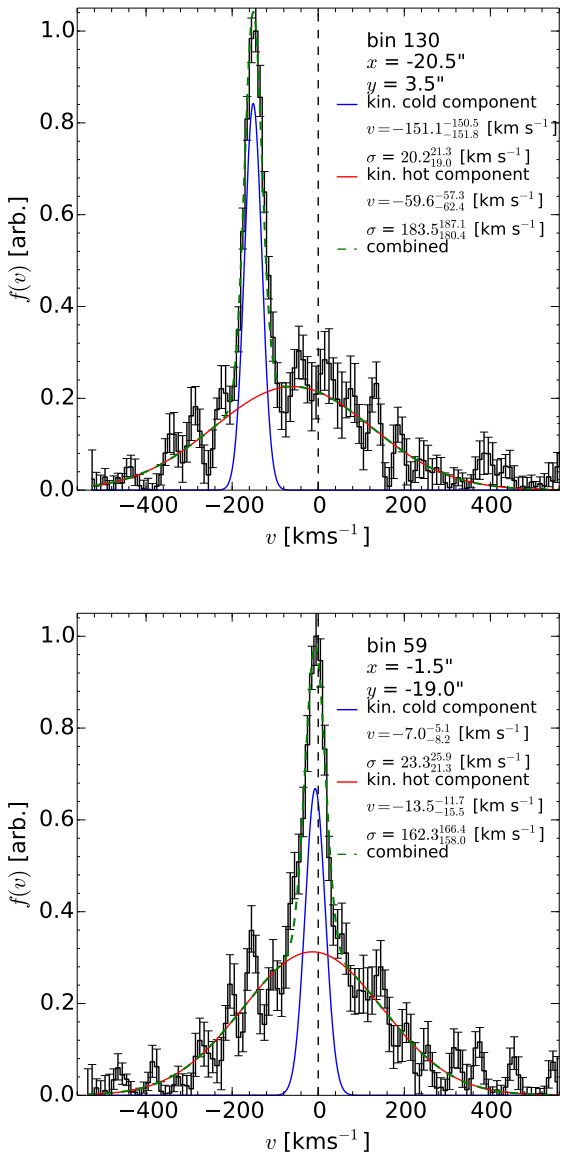

Figure 3. Examples of two recovered line-of-sight velocity distributions and their double-Gaussian decompositions. The upper panel shows the distribution for bin 130, which is located along the major axis at a radius of about 20″ (compare Fig. 2). The red and blue lines show our best fitting double-Gaussian decomposition of the LOSVD. The vertical dashed line shows the systemic velocity, which we set to zero. The lower panel shows the same for a position along the minor axis located about 19″ away from the nucleus.

similar approach to Scorza & Bender (1995) we fit a double-Gaussian distribution

$$f(v) = \frac{A_{cold}}{\sigma_{cold}\sqrt{2\pi}} e^{\frac{-(v-\mu_{cold})^2}{2\sigma^2_{cold}}} + \frac{A_{hot}}{\sigma_{hot}\sqrt{2\pi}} e^{\frac{-(v-\mu_{hot})^2}{2\sigma^2_{hot}}} \quad (1)$$

to the LOSVDs $f(v)$, where A_{cold} and A_{hot} are the relative weights of each component, μ_{cold}, and μ_{hot} are their mean velocities and σ_{cold} and σ_{hot} are their velocity dispersions. The labels *hot* and *cold* denote the higher and the lower velocity dispersion component respectively. We optimize the fit using the least square fitting routine `lmdif` of the MINPACK package (Moré, Garbow & Hillstrom 1980). The fit is degenerate as a priori it is not clear which of the two Gaussians should represent which of the two components. In practice we inspect every fit by eye and adjust the starting parameters of the fit so as to yield smoothly varying velocity fields. The fits are nevertheless very stable and, with the exception of the actual assignment of the two Gaussian distributions to either of the two components, we find little dependence on the starting values. We repeat the fit to all 30 LOSVDs that result from the Monte Carlo simulations to estimate errors on the best fitting parameters.

4.4 Mg and Fe indices of the two kinematic components

In the previous sections we presented evidence that there are two distinct kinematic components in NGC 7217. Here we study the properties of their stellar populations to constrain their formation mechanisms. If these two components formed at different epochs or from different gas sources, we would also expect to find differences in their chemical content.

We apply the spectral decomposition technique that was introduced in Coccato et al. (2011b, 2013), which allows us to separate the spectra of the two kinematically distinct components in the observed galaxy spectrum. The algorithm is based on pPXF (Cappellari & Emsellem 2004) but allows for two separate velocity distributions that are fit simultaneously. The model spectra for the two kinematic components are built independently from a linear combination of stellar templates that are convolved with either of the two LOSVDs. In this way, the code allows the two kinematic components to have different stellar population properties. The LOSVDs are parametrized by Gaussian functions with different velocities and velocity dispersions. After the optimisation, the best-fitting linear combination of stellar templates represents the stellar populations of the two kinematic components, and therefore allows us to investigate their stellar populations separately. This method is complementary to the technique of the recovery of the full LOSVD and subsequent decomposition that we presented in the previous two sections. In principle it therefore adds a completely independent kinematic analysis as well as a chemical analysis.

The covered wavelength range allows us to measure the equivalent widths of the Mg *b*, Fe5270, and Fe5335 Lick indices, as defined by Worthey et al. (1994). Because of the lack of Balmer absorption lines, we cannot derive the ages of the two stellar components. Nevertheless, the measurement of Mg and Fe, still provides important information on the chemical composition of the different stellar components.

We proceed as follows: the direct spectral decomposition requires a larger signal-to-noise ratio than the previous method. We therefore adopt a more aggressive spatial binning than that of Section 4.2. Our Voronoi bins reach $S/N \geqslant 90$ per spectral pixel and per bin.

In contrast to previous studies (Coccato et al. 2011b, 2013; Johnston et al. 2012), our data's relatively small wavelength range introduces degeneracies to the simultaneous fit of kinematics and stellar populations. In general, the kinematic moments that we recover using either of the two

Table 2. Offset to the Lick indices.

Index	Mean Offset [Å] (1)	Error [Å] (2)
Mgb	−0.04	0.25
Fe5270	0.47	0.20
Fe5335	−0.92	0.17

Notes– Col. 1: Mean offset; offsets are defined as the difference between values (Worthey et al. 1994) and our measurements. Col. 2: Standard deviation of the measured offsets.

methods are in excellent agreement, independent of the initial guesses. However, the ambiguity in the computation of the best-fitting templates is too high to reliably constrain the line strength indices. In a similar approach to Katkov, Sil'chenko & Afanasiev (2013), we therefore use the kinematic information determined in Section 4.3 to constrain the velocities and velocity dispersions of the two components. This lowers the number of free parameters and removes much of the degeneracy, as demonstrated by a series of Monte Carlo simulations (see Section 5.3).

To perform the spectral decomposition, we use the stars in Table 3 flagged with 'S', which cover the (Mg b,⟨Fe⟩) plane. These stars provide a better fit to the galaxy spectra than the stars from other stellar libraries in the literature (e.g. ELODIE Prugniel & Soubiran 2001), probably due to subtle differences in the spectral line spread functions of the libraries and our data.

The spectral decomposition code returns the spectra of the two best-fit templates that are associated with the two kinematic components. We broaden these spectra to match the 8.4 Å instrumental resolution of the Lick System (Worthey & Ottaviani 1997), and we then measure the equivalent width of the Mg b, Fe5270, and Fe5335 absorption line indices. The systematic offset to the Lick System is computed and corrected using the stars in our library in common with (Worthey et al. 1994), which are marked by 'L' in Table 3. The measured offsets are listed in Table 2. The offsets are constant within the range defined by the measurements. We do not apply any correction for the Mg b index as the mean of the offsets is smaller than their standard deviation.

5 RESULTS

5.1 Stellar and ionized-gas kinematics

In this section we describe the results of the kinematic fit (Section 4.2 and Section 4.3) and the double-Gaussian decomposition (Section 4.4).

In Fig. 4 we plot the full line-of-sight velocity distributions along lines of constant dec and RA. The vertical axis is velocity and the horizontal axis is the spatial position. The constant dec cut (upper panel) falls close to the major axis because the major axis of NGC 7217 is closely aligned with the east-west axis. One immediately identifies a rapidly rotating component with a relatively low velocity dispersion. The rotation curve rises steeply in the centre and flattens out at a radius of 20″. The rotation amplitude reaches about 150 km s^{-1}. The white areas in that

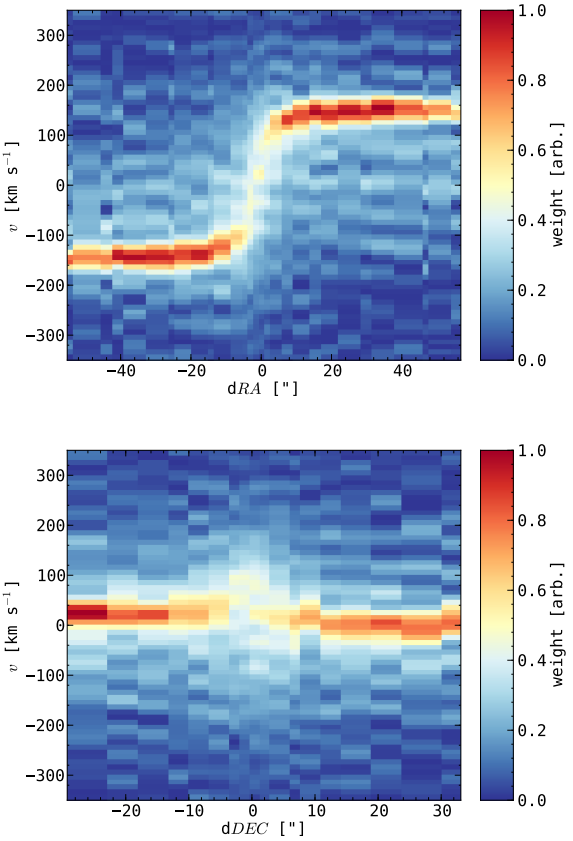

Figure 4. Recovered line-of-sight velocity distributions along cuts of constant dec (upper panel) and RA (lower panel) through the centre of the galaxy. We recover the LOSVD for each spaxel of our datacube as described in the text. The y-axis shows velocity channels with the systemic velocity subtracted. We restrict the plot to velocities of ± 350 km s^{-1}.

panel show another component with a much larger velocity dispersion. One may compare this figure to Fig. 3, which shows individual LOSVDs that correspond to vertical cuts in Fig. 4. There the broader underlying component is even more easily identified. Similarly, the plot along constant RA (lower panel) shows a narrow component close to zero velocity and a much broader component underneath. The upper panel shows no sign of a counter-rotating disk. Such a disk would show up as an opposite s-shape structure. Similarly, Fig. 3 does not show an additional low-dispersion peak that would have to be located at about 150 km s^{-1}.

We therefore find no evidence for a counter-rotating disk. Rather we find one low-dispersion disk that is embedded in a high-dispersion component that shows little rotation.

It is more difficult to estimate the amount of rotation of the hot component from Fig. 4. We therefore turn to the results from the decomposition shown in Fig. 5. From left to right, this figure shows the amplitude, the mean velocity and the velocity dispersion of the best-fitting Gaussian. The upper two rows show the parameters for the low and high dispersion stellar components, while the bottom row shows the parameters for gas visible in [O III] emission. The

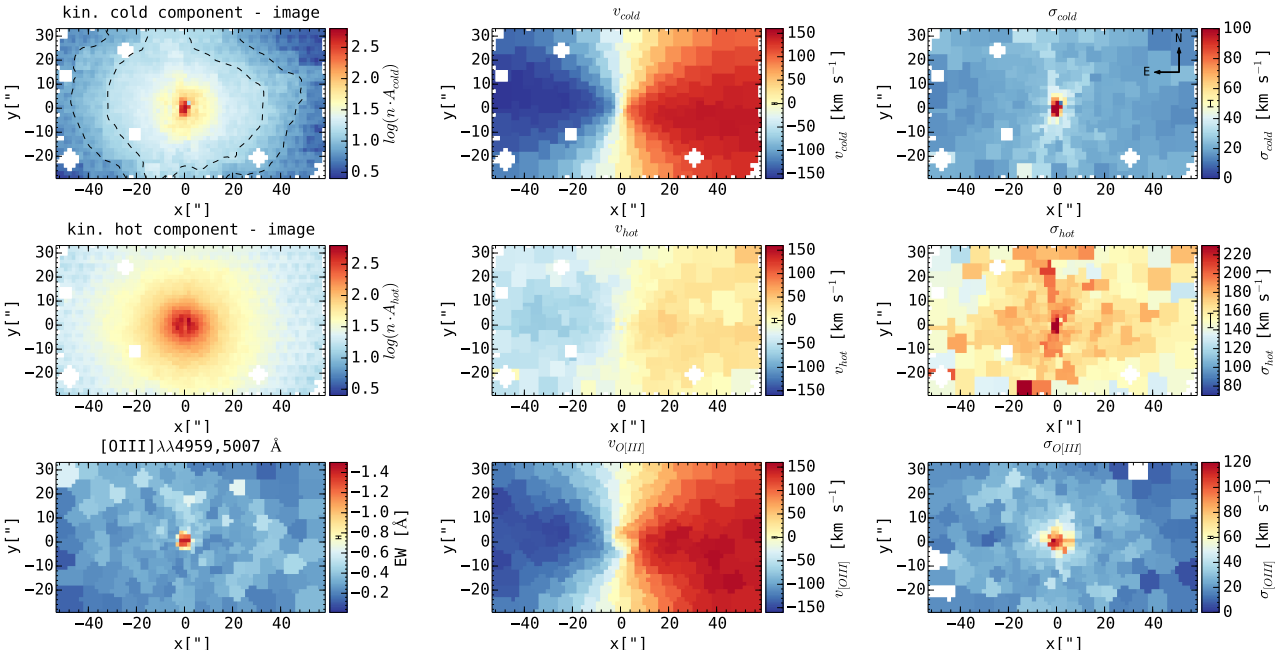

Figure 5. Two-dimensional maps of the of the stellar kinematics obtained from the double-Gaussian decomposition and the gas kinematics. We decompose the recovered line-of-sight velocity distributions into two Gaussians (compare to Fig. 3) and plot from left to right: the amplitude, the mean velocity and the velocity dispersion of the best fitting Gaussian model. The upper row plots the moments for the cold component while the middle row plots the hot component. The amplitudes for the two components have been normalized such that their integrated sum equals the wavelength collapsed datacube (see text). To highlight the flattening of the cold disk component, we added contours at two arbitrary values. We caution the reader that the decomposition becomes degenerate inside of a radius of 3″, due to the relatively low weight of the kinematic cold component and the limited spatial resolution of VIRUS-W. The bottom row shows the summed equivalent width of the [O III]λλ 4959,5007 Å emission lines and the velocity and velocity dispersion obtained by the kinematics extraction routine from the brighter line at 5007 Å. In all maps positive y-values point to north and positive x-values to west.

fitted amplitudes (parameters A_{hot} and A_{cold} in equation 1) correspond to line strength and therefore give little information on the spatial extent of the two components. We therefore scale them by enforcing the sum of the two amplitudes to equal the signal of the collapsed datacube. We collapse the datacube in an emission line free region redwards of the Mg b feature (rest frame 5230 Å–5400 Å). The results are *images* of the two components as they would appear if they could be observed separately. It is these component images that are shown on the left of Fig. 5. As the fiber size of VIRUS-W is 3.2″ and, because the low dispersion component has relatively low weight at the nucleus, the decomposition becomes unreliable inside a radius of 3″. We nevertheless plot the innermost values for completeness. The component images suggest that the light distribution of the cold component is flatter than that of the high dispersion component. Also it appears more elliptical in shape and aligned with the major axis position angle. The cold component typically contributes 20%–40% of the light outside the central 8″. In the next section we fit two-dimensional surface brightness models to derive scale lengths and ellipticities of the two components.

The velocity fields of the two components show that they are actually co-rotating. The rotational amplitude of the cold component reaches 150 km s^{-1} while the dispersion stays mostly flat at 20 km s^{-1} throughout the field of view. In contrast, the hot component reaches a rotational amplitude of 58 km s^{-1} and its dispersion rises from ≈ 150 km s^{-1} at the edges of the field of view to ≈ 170 km s^{-1} in the central regions.

The kinemetry IDL routine (Krajnović et al. 2006) shows that the velocity fields have best fitting position angles of $82.7 \pm 2.0^{\circ}$ and $80.6 \pm 3.8^{\circ}$ for the cold and the hot components respectively (three sigma errors).

5.2 Structural parameters

In the previous section we reconstructed images of the two kinematic components as they would appear if they could be observed separately. For this the relative amplitudes from the double-Gaussian decomposition are scaled, such that their sum equals the integrated flux in an emission line free waveband. With these results we can now attempt to derive structural parameters for the two individual components and to compare them to the values that are derived from photometry. We use the `Imfit` package[1] by Erwin (2014) to fit two-dimensional models to respective images.

Following B95, we model the cold component with an exponential disk but also include a Gaussian ring to account for the inner stellar ring. As in B95, we adopt a de Vaucouleurs' law for the surface brightness distribution of the hot stellar component. We use the formal errors from the double-Gaussian decomposition to create error images for `Imfit` and mask the positions of foreground stars.

[1] http://www.mpe.mpg.de/∼erwin/code/imfit/

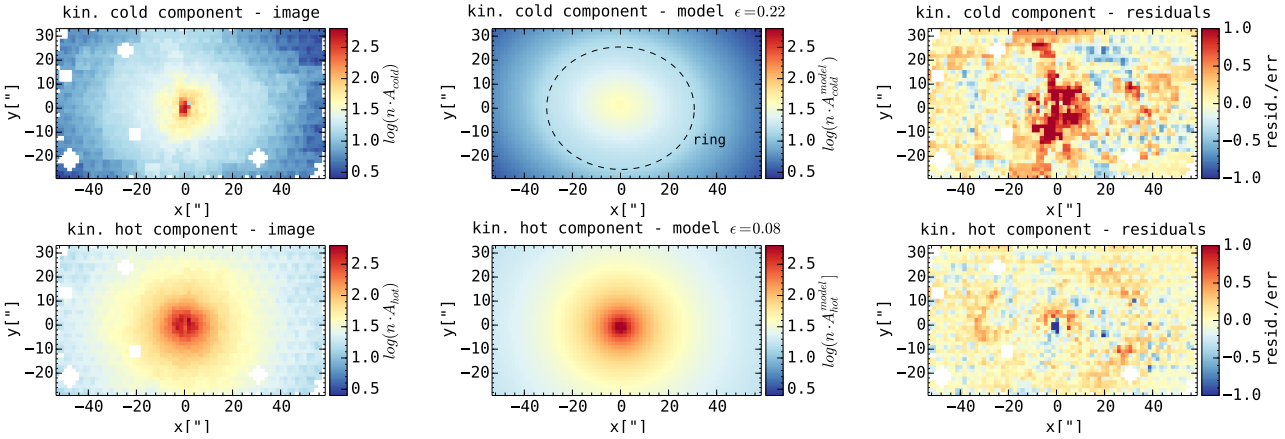

Figure 6. Two dimensional models of the kinematic components in NGC 7217. The *images* of the two separate components are obtained through the double-Gaussian decomposition and proper scaling as described in the text. We reproduce the images of the two components from Fig. 5 on the left. We fit an exponential disk model to the low dispersion component and also include a Gaussian ring to account for the inner stellar ring. We model the kinematically hot component with a de Vaucouleurs' profile. The two best fitting models are shown in the middle column. The dashed line marks the location of the ring in the model for the cold component. The right columns shows the residual maps. The central $r > 15''$ of the cold component were excluded from the fit as they were poorly matched by an exponential light distribution.

In Fig. 6 we reproduce the component images from Fig. 5 on the left, the best fitting model in the middle column, and the residuals on the right. The central $20''$ of the model of the hot component shows positive residuals. As the decomposition is degenerate in the central region, we mask the corresponding area and constrain our fit to the to data with $r > 15''$. We also fix the centre of both components to the brightness centre that we determine from the collapsed datacube. We allow for a variable flat sky background for the cold component. We find that this is necessary for the fit to converge to reasonable values. This may be due to imperfect sky subtraction, which is perhaps not surprising given our reliance on sky nods for background subtraction.

We give our best fitting parameters in Table 3. We cannot quote central surface brightnesses or effective surface brightnesses as our data are not flux calibrated.

Table 3. Structural parameters of the two kinematic components

Parameter	Value	Uncertainty
Cold component — exponential disk		
Position angle [°]	82.1	± 2.5
ellipticity	0.23	± 0.02
h [″]	43.19	± 1.2
D/T	0.221	
Cold component — Ring		
Position angle [°]	88.7	± 10.8
ellipticity	0.17	± 0.07
radius [″]	30.7	± 1.3
width σ [″]	4.2	± 1.0
R/T	0.005	
Hot component — de Vaucouleurs		
Position angle [°]	85.8	± 7.9
ellipticity	0.08	± 0.02
r_e [″]	58.1	± 11.9
B/T	0.774	

Notes– D/T is the ratio of the total model flux in the cold disk component to the total flux of all components. R/T is the relative flux in the inner stellar ring model and B/T is the relative flux in the model of the hot stellar component.

5.3 Direct decomposition & line strength analysis

In Fig. 7 we show the two-dimensional maps of the equivalent width of Mg *b*, Fe5270, and Fe5335 for the two stellar components. We use a set of Monte Carlo simulations that match the observational setup (wavelength coverage, spectral resolution and sampling, signal-to-noise) and the mean galaxy characteristics (velocity separation between the two components, stellar velocity dispersion, flux) to compute the uncertainty on the measured Lick indices. The mean uncertainties from the simulations are about 0.2 Å and 0.1 Å for the indices of the cold and the hot component respectively. In addition, these simulations show that the errors on the Lick indices would have been > 2Å, if we had not used the constraints on the kinematics derived in Section 4.3. In other words, the spectral decomposition code with the given instrumental setup, needs independent kinematic measurements to remove the degeneracy when recovering the best fitting stellar templates. The same results are shown in Fig. 8, where the measurements are plotted in the $(\mathrm{Mg}\, b, \langle \mathrm{Fe} \rangle = (\mathrm{Fe5270} + \mathrm{Fe5335})/2)$ plane and compared to the predictions of single stellar populations models. The two components have different line strengths: the cold component has significantly lower values of Mg *b*, and significantly higher values of Fe5270 and Fe5335 than the hot component.

We note a systematic trend in the measurements: the west side of the galaxy has higher values than the east for all indices. This effect, of unknown cause, is evident in the fainter cold component and negligible in the brighter hot

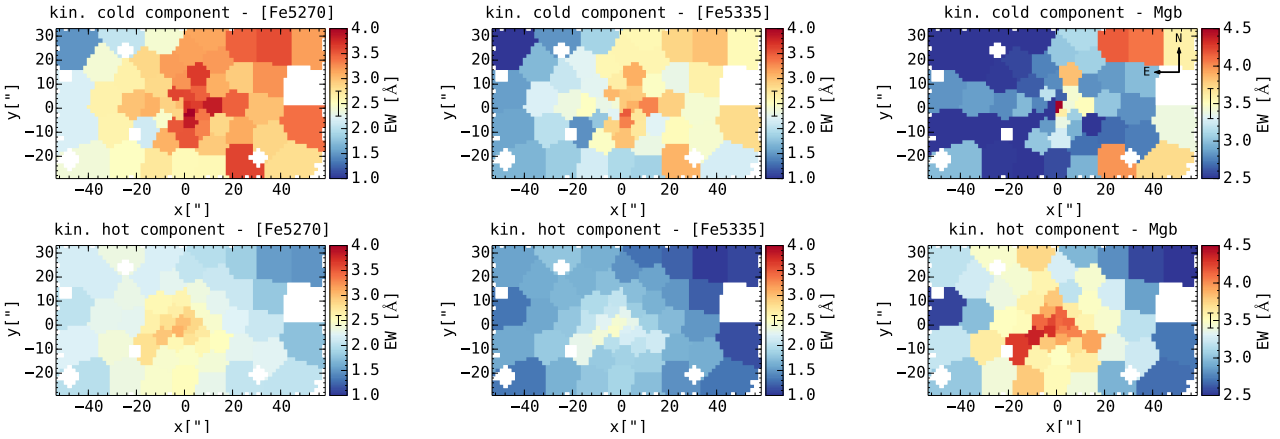

Figure 7. Two-dimensional maps of line strength indices, calibrated to the Lick system, for the cold (top panels) and hot stellar (top panels) components. The vertical bars in the color scale indicate the mean uncertainty as obtained from the MC simulations.

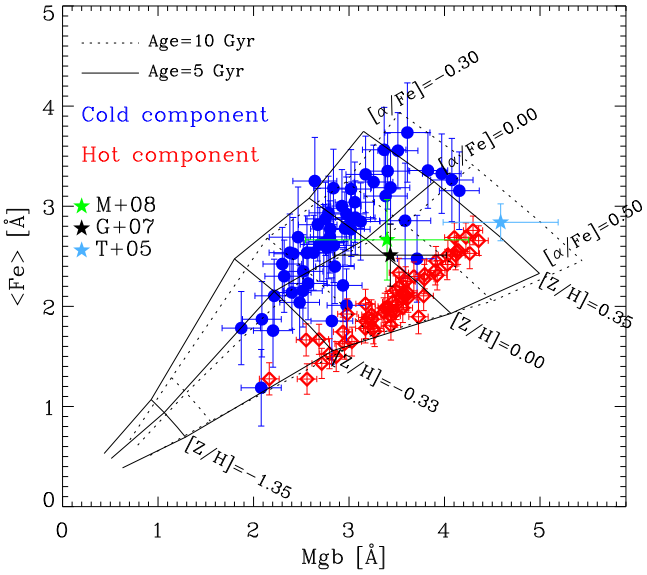

Figure 8. Mg*b* and ⟨Fe⟩ line strengths indices measured for the cold component (blue circles) and the hot component (red diamonds) in NGC 7217. Predictions from single stellar population models (Thomas, Maraston & Bender 2003a) are also shown for comparison. The black, and green stars represent the mean values of the measurements by Gorgas, Jablonka & Goudfrooij (2007) and Morelli et al. (2008) for a sample of bulges in spiral galaxies with the corresponding error bars representing the standard deviations of their measurements. The light blue star and its error bars represents the mean measurements and the standard deviation of a sample of early-type galaxies by Thomas et al. (2005).

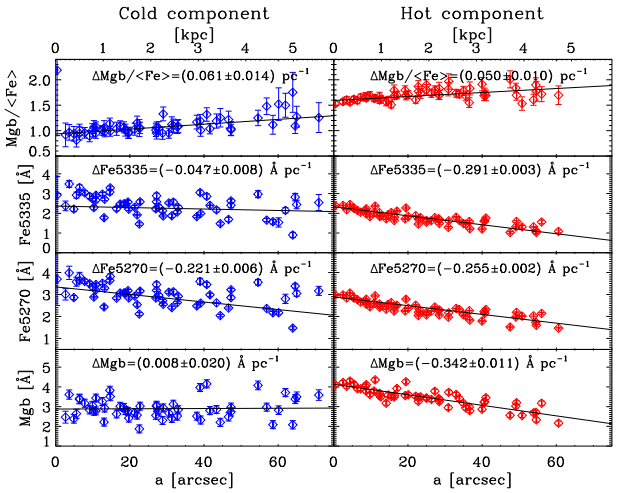

Figure 9. Line strength indices of the cold component (left panels) and the hot component (right panels), as a function of radius. The black lines are linear fits to the data. The gradients of the fits are shown in the panels.

component, and explains the large scatter in the measurements observed for the cold component (see Fig. 8). Nevertheless, this systematic trend is smaller than the observed difference between the two kinematic components in the (Mg *b*,⟨Fe⟩) plane, and does not invalidate our results.

The two components also show a radial gradient in the measured indices (Fig. 7): central regions have higher values of the Fe and Mg *b* equivalent widths (see also Fig. 9). Radial gradients are more evident in the hot component than in the cold because of the larger scatter and systematic trend present in the latter. The corresponding gradients are shown in the figure.

6 IONIZED GAS KINEMATICS AND TILTED RING ANALYSIS

The velocity field of the [O III] emission shows a striking resemblance to that of the cold component. The velocity dispersion of 20km s^{-1} to 30km s^{-1} is also similar to the values found in the cold component. However, within a radius of 6″ the velocity field of the gas shows a strong twist. Sil'chenko & Afanasiev (2000) claim the existence of a nuclear polar gas ring in NGC 7217 that may be responsible for this twist. We now investigate this scenario in detail.

We construct a tilted ring model to reproduce the ionized gas kinematics under the assumption of purely circular

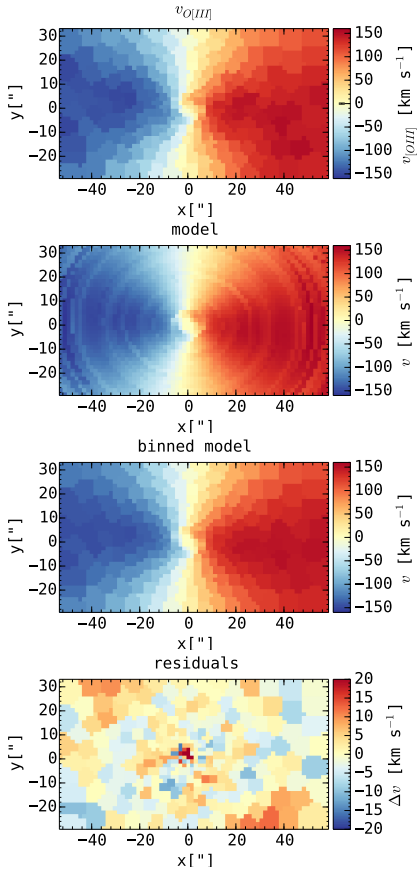

Figure 10. Tilted ring model for the gas disk. The upper panel reproduces the mean line-of-sight velocity of the [O III] emission from Fig. 5. We fit a series of 45 rings with a radial spacing of 1.6″. We sample each ring every 2° and project the line-of-sight component of the circular velocity into the pixel grid. The fitted parameters are the relative weight of a ring, its position angle on the sky, its inclination angle and the circular velocity. The fit is carried out in two stages as described in the text. The best fitting parameters are plotted in Fig. 11. The second panel shows our best fitting model. The third panel shows the model after the application of the same Voronoi binning scheme that we use for the data. The bottom panel shows the residuals.

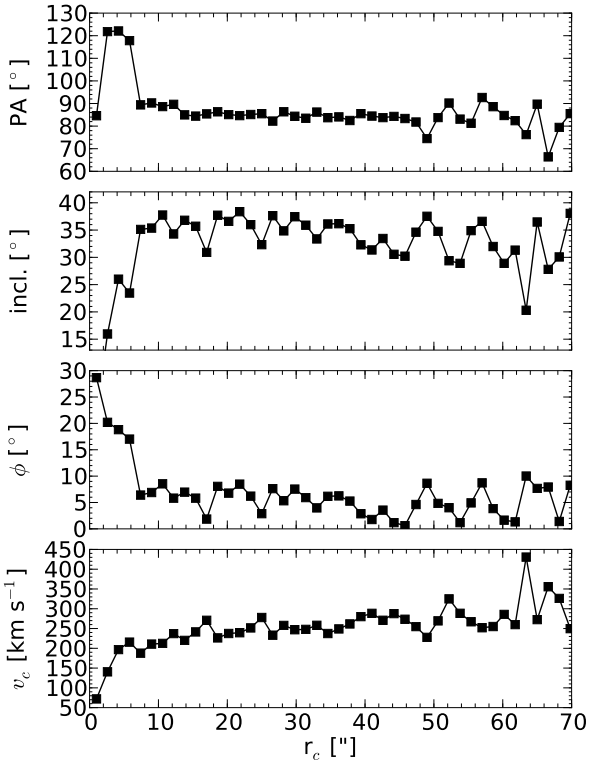

Figure 11. The best fitting parameters for the tilted ring model that is shown in Fig. 10. The upper two panels plot the projected position angle on the plane of the sky and the inclination angle for all rings. The third panel shows the angular separation between the corresponding axis of rotation and the axis of the rotation of the best fitting global thin disk model that we derived in the first stage of our modelling. The lowermost panel shows the circular velocity as function of ring radius.

motion. The model consists of 45 rings equally spaced in radius that are projected onto the sky plane. The free parameters for each ring are: its relative weight, the observed position angle, the inclination, and the circular velocity. We project those rings onto the same pixel grid that we use for the binning of our observed data and also compute mean velocities in the same Voronoi bins as we use for the observations. We fit the model in two stages. First we tie the position and inclination angles as well as the circular velocities of all rings to each other which effectively results in a simple thin disk model. We then optimize these three free parameters (the weight is fixed to one in the disk model) for minimal χ^2. This already generates a very good model for the gas disk velocities outside of the central 15″ with residuals that seem to be dominated entirely by noise. The best fitting parameters are PA $= 84.6 \pm 0.6°$, $i = 33.9 \pm 1.2°$ and $v_c = 260.3 \pm 6.8\,\mathrm{km\,s^{-1}}$.

In the second stage we now untie the relative alignment and the circular velocities and rerun the fit — again minimizing for χ^2 — while using the best-fit parameters from the first stage as initial guesses. In Fig. 10 we reproduce the gas velocity field from Fig. 5 and show plots of the best fitting model and a map of the residuals. The third panel shows the Voronoi-binned velocity map of the model. The central twist is reproduced well by the tilted ring model.

Using the parameters from the thin disk model, we derive the angular separation ϕ of the rotation axis of the inner rings with respect to the rotation axis of the outer disk. Fig. 11 shows the parameters that we derive for the titled rings as a function of the ring radius. From top to bottom, the panels show the projected position angle, the inclination, the angular separation and the circular velocity. From our data the maximum angular separation of the inner rings with respect to the outer disk is 30°. This is significantly lower than the 90° that would imply a polar ring, and it resembles more an inner warped gaseous structure, as observed, for example, in the spiral galaxy NGC 2855 (Coccato et al. 2007).

If the central regions of NGC 7217 do host a non-axisymmetric structure, as suggested by B95, then an alternative explanation to the observed twist may lie in non-circular motions of the gas due to a corresponding non-

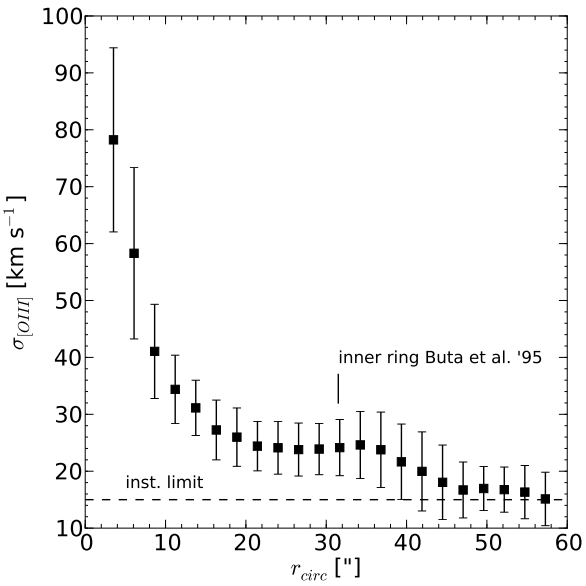

Figure 12. Velocity dispersions of the [O III] emission line as a function of radius. We derive the mean dispersion in elliptical annuli. The ellipticity of the annuli is set to 0.2. The horizontal axis plots the length of the semi-major axis. The error bars show the variation of the gas dispersion within each annulus. These dispersions have been corrected for the instrumental resolution by subtracting 15 km s^{-1} in quadrature. The horizontal dashed line indicates the resolution limit.

axisymmetry of the potential (e.g. de Zeeuw & Franx 1989; Athanassoula 1992).

We find a slight increase in the gas dispersion at the location of the inner ring. This is best seen in Fig. 12 where we plot the averaged gas dispersion in elliptical annuli with an ellipticity fixed to the value of 0.2 and a position angle of 85°. B95 gives a radius of 32″ for the inner ring. The dispersion profile does show a shelf or a hump at about the same location and falls off to ≈ 15 km s^{-1} — which is just the instrumental resolution limit — at a radius of 45″. Inside the ring, the dispersion rises continuously to about 80 km s^{-1} at 3″, which is within the radius our measurements become unreliable due to their limited spatial resolution.

7 DYNAMICAL MASS TO LIGHT RATIO COMPARED TO STELLAR POPULATION ANALYSIS

In the last section we saw that the ionized gas in NGC 7217 shows very regular rotation outside of $r \approx 5''$ with a deprojected velocity of 200 km s^{-1}. In Section 5.1 we measure velocity dispersions ≈20 km s^{-1}. The gas disk is therefore well approximated by a cold and thin disk and we can directly derive the total gravitating mass enclosed in a sphere of a given radius. On the other hand, the inner dust ring ($r \approx 10.5''$) marks a strong transition from the outer dusty spiral morphology to a relatively dust free central region giving a relatively unperturbed view of the central stellar population (Fisher & Drory 2008, see also Fig. 1), which is presumably dominated by the spheroid.

We can therefore attempt to derive a stellar mass-to-light ratio from a stellar population analysis, and compare this value to the dynamical measurement. We obtained archival SDSS *ugriz*-band images (York et al. 2000), FUV and NUV GALEX (Martin et al. 2005) data from Mikulski Archive for Space Telescopes, and Spitzer IRAC channel 1 to 4 data (Werner et al. 2004; Fisher & Drory 2010). We measure the mean flux in an aperture of diameter 10″ centered on the galaxy and estimate the background in empty regions outside of the galaxy. The 10″ aperture stays clear of the dust ring even in the lower resolution GALEX data. We correct all images for galactic foreground extinction using an $E(B-V)$ of 0.0761 (Schlafly & Finkbeiner 2011 recalibration of Schlegel, Finkbeiner & Davis 1998). We then use the updated 2007 version of the Bruzual & Charlot (2003) models for single-aged stellar populations to invert the colours into stellar population parameters and, in particular, to derive mass-to-light ratios. As the models are relatively coarsely spaced in metallicity, we interpolate the predicted fluxes between metallicity values linearly, adding three equally spaced metallicity values between the published quantities. For each of the resulting models we compute the χ^2 between the predicted magnitudes and the measured values assuming an error of ±0.15 mag in the GALEX bands (Gil de Paz et al. 2007) and ±0.05 mag in the other bands. The best-fitting model is chosen based on the minimum χ^2 value and the errors are estimated by considering the maximum and minimum values of all models that have $\Delta\chi^2 = 1$. The IRAC 4 magnitudes were typically poorly fit which may be a consequence of the poorer resolution in this band and an onset of the contribution from dust emission. We exclude this band from the fit.

The GALEX channels are particularly important to break the age/metallicity degeneracy. Without those data models with $[Z/H] = 0.0$, 0.1 and 0.2 give similarly low χ^2 vales with very little constraint on the mass-to-light ratio. Adding the GALEX data however results in a clear preference of $[Z/H] = 0.2$, yielding a V-band mass-to-light ratio of $\Upsilon^*_V = 3.9^{4.3}_{3.7} M_\odot/L_\odot$ and an age of $7.5^{8.3}_{7.2}$ Gyr if a Kroupa Initial Mass Function (IMF; Kroupa 2001) is assumed. For a Salpeter IMF (Salpeter 1955) we obtain values of $\Upsilon^*_V = 6.1^{7.2}_{5.9} M_\odot/L_\odot$ and an age of $7.5^{10}_{7.2}$ Gyr. We do have an independent estimate of the metallicity from the line strength analysis in Section 5.3. By comparing Fig. 9 and Fig. 8 one can see that for the central Mg and Fe line strengths of the hot component, the adopted Thomas, Maraston & Bender (2003b) models predict metallicities between $[Z/H] = 0.15$ assuming a 10 Gyr old population and $[Z/H] = 0.3$ when assuming a 5 Gyr old population. This range of metallicities is compatible with the photometrically derived value. Adding this constraint to our parameter inversion while dropping the FUV/NUV bands results in essentially identical predictions of the stellar mass-to-light ratio and ages.

To determine the dynamical mass-to-light ratio, we evaluate the gas rotation curve of our tilted ring model in the previous section at a radius or 6″. This is slightly larger that the aperture size we used for the stellar population analysis but puts the analysis slightly more comfortably outside of the twist in the velocity field. Using the Tully-Fisher based distance estimate of $D = 18.4$ Mpc (Russell 2002) and a

velocity of $200 \pm 10\,\mathrm{km\,s^{-1}}$ we obtain a dynamical mass of $5.0 \pm 0.5 \times 10^9\,M_\odot$ inside a radius of 535 pc.

In the central regions of a stellar system, any aperture photometry necessarily integrates also over the whole light in a cylinder with the radius of that aperture. In order to compute the true dynamical mass-to-light ratio, one must find the actual fraction of light that is contained inside of a sphere of the radius at which the rotational velocity is determined. For this we deproject the analytical model of the V-band surface brightness profile of B95 for the spheroid. The deprojection is carried out axisymmetrically using the code of Magorrian (1999). Using the magnitude of the sun of $V = 4.83$ Binney & Merrifield (1998) and an extinction of $A_V = 0.24$ (Schlafly & Finkbeiner 2011) we derive a luminosity of $1.1 \times 10^9\,L_\odot$ or dynamical mass-to-light ratio of $\Upsilon^*_{\mathrm{dyn}} = 4.5 M_\odot/L_\odot$. This value is marginally larger than the mass-to-light ratio that we derive from the stellar population analysis for a Kroupa IMF and smaller than the values expected for a Salpeter IMF. Given the central velocity dispersion of 150–170 $\mathrm{km\,s^{-1}}$ this is in excellent agreement with relations derived for early-type galaxies (Treu et al. 2010; Thomas et al. 2011; Cappellari et al. 2013).

8 DISCUSSION

8.1 Stellar co vs. counter-rotation

We do not confirm the existence of a counter-rotating disk that was previously claimed. The shape of our derived LOSVDs and the kinematic decompositions rather suggest that NGC 7217 hosts a sub-dominant cold stellar component co-rotating with a bright hot stellar component.

In Sil'chenko & Afanasiev (2000) the rotation curve along PA = 240° is shown. Their rotation curve, derived using the absorption line feature [Na I]$\lambda\lambda$ 5890,5896 Å shows counter-rotation within the central 40″ (their Fig. 6). The main stellar component rotates slowly and appears asymmetric. It reaches a maximum amplitude of $\approx 100\,\mathrm{km\,s^{-1}}$, and then stays flat at $R > 30''$, and declines at $R < -30''$. The asymmetry in the counter-rotating component is even larger and reaches an amplitude of $\approx 300\,\mathrm{km\,s^{-1}}$ at $R < -10''$ but only $\approx 200\,\mathrm{km\,s^{-1}}$ for $R > 10''$.

While they do not derive rotation curves, Merrifield & Kuijken (1994) originally found counter-rotation based on their detailed analysis of individual velocity distributions. The authors did consider the contamination by a very massive bulge component as explanation for their observed tail in the absorption line profiles but rejected that hypothesis based on the argument that such a hot component had not been observed and would be atypical for a disk galaxy with spiral structure. Through deep photometry B95 however showed the presence of such a halo and argued that the relative luminosities are in the right order to generate the observed profiles. Our kinematic confirmation of a hot halo now further completes this picture.

However, the velocity distributions presented by Merrifield & Kuijken (1994) in their Fig. 6 do show a distinctive secondary peak that cannot be explained by a bulge contamination. We can only speculate at the reason for this secondary peak: first, their data are long slit spectra which prohibit two dimensional binning. Compared to their Fig. 3, the Voronoi bins of our IFU data have significantly higher S/N at the important radial range of the two-component overlap. Second, their data have a spectral resolution of $\sigma_{\mathrm{instr}} \approx 25\,\mathrm{km\,s^{-1}}$ (measured at 5200 Å), and the authors rebinned their spectra in $[\ln\lambda]$ to have a velocity step of $28.5\,\mathrm{km\,s^{-1}}$ per pixel. In comparison, our data have a spectral resolution of $15\,\mathrm{km\,s^{-1}}$ and we bin our spectra in $\ln\lambda$ with a velocity step of $10\,\mathrm{km\,s^{-1}}$ per pixel. The resolution of our spectra therefore allows a cleaner separation of the two components. Finally, Merrifield & Kuijken (1994) do not adopt any special treatment of emission lines, which might affect the shape of their derived LOSVDs.

The resolution argument also applies to the work of Fabricius et al. (2012b). There a similar double-Gaussian decomposition of FCQ-derived LOSVDs suggested a dynamically hot, counter-rotating component. However, the spectral resolution of that work was $39\,\mathrm{km\,s^{-1}}$, which is significantly lower than the resolution used here.

We test that our results are not driven by systematics in the non-parametric kinematic fit by cross-checking with the parametric spectral decomposition technique of Coccato et al. (2011b). We use starting guesses that resemble two counter-rotating disks, as found by Merrifield & Kuijken (1994). The best fit solution found by the spectral decomposition code is still consistent with a cold disk co-rotating with a hot stellar component, as found in Section 5.1. Further, our code allows us to force the fit to two counter-rotating disks by locking their mean rotational velocities to be the opposite with respect to the systemic velocity. In Fig. 13 we compare the actual best-fitting solution from the spectral decomposition (upper panel) with the enforced counter-rotation solution. In that example the enforced counter-rotation results in a RMS that is increased by a factor of two over the non-constrained fit.

We stress the fact that both routines, i.e. the algorithm for the recovery of non-parametric LOSVD with subsequent double-Gaussian decomposition and the method of the direct spectral decomposition, are completely independent. They both use their own treatment of the stellar continuum and use different strategies for the derivation of the optimal model spectrum.

8.2 Structural parameters through kinematic decomposition

In Table 3 we list the structural parameters for the two kinematic components. A kinematic double-Gaussian decomposition cannot be expected to yield the same precision as a photometric decomposition. But by comparing our values to the photometric data we can conclude that our two components correspond to the stellar disk and the spheroid that were inferred by photometric decomposition in B95.

Our derived values of the position angle are in reasonable agreement with the value of 91° from B95. In the radial range of $30'' \leqslant r \leqslant 120''$, our values for the ellipticity bracket their values of about 0.3 (their Fig. 6), which is expected given that they measure the ellipticity of the superposition of the two components. For $r > 140''$ B95, find an ellipticity of about 0.05 with some variation, which is compatible with our findings.

For the spheroid, we find an effective radius of $58.1 \pm 11.9''$ which compares to the V-band value of $49.9 \pm 3.4''$ by

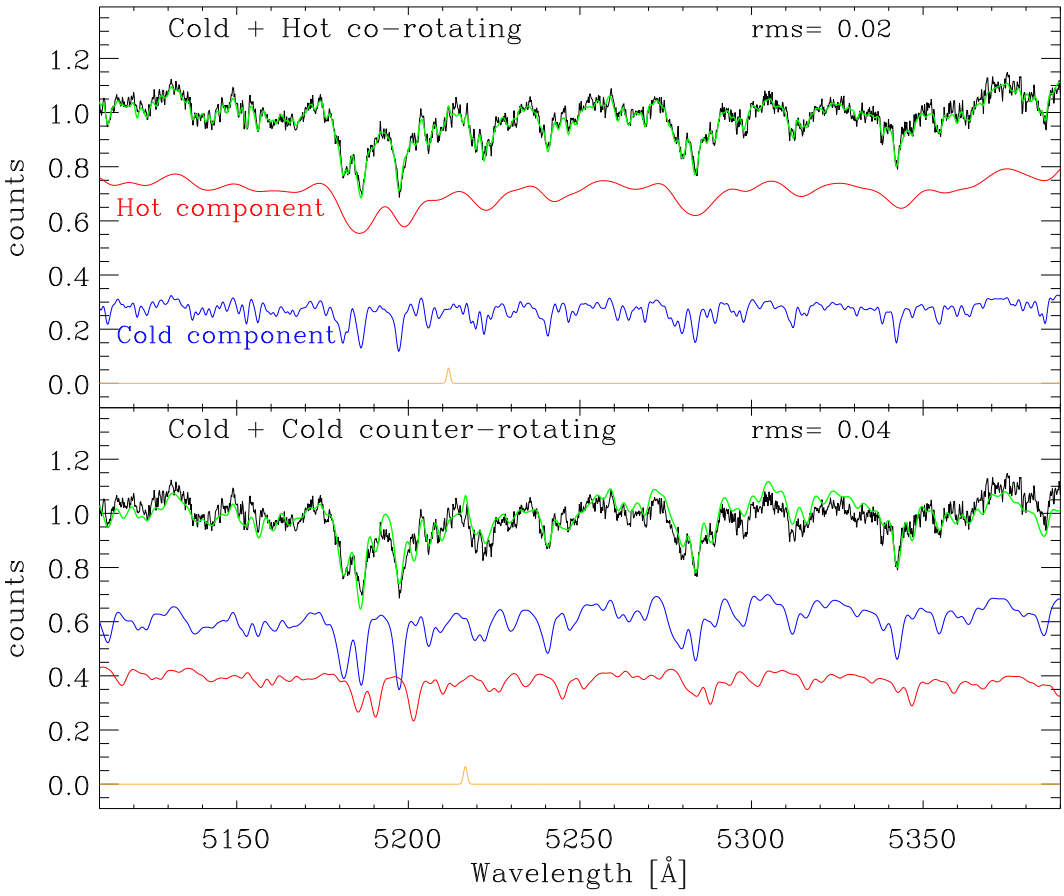

Figure 13. Results of the spectral decomposition code. In both panels we show the actual data in black, while the best-fitting two components are plotted in red and blue. The green line shows the sum of those two components. The orange line shows the best-fitting model for the nebular emission. In the upper panel we show the actual best fit, while in the lower panel we enforce a counter-rotating disk scenario as suggested by Merrifield & Kuijken (1994).

B95. For the scale length of the exponential disk we obtain $43.2 \pm 1.2''$ vs. B95's $29.7 \pm 2.0''$.[2] The difference in the effective radii and scale radii are easily explained by the much lower resolution and coverage of our component images. The general shape of the radial distribution seems, however, to be in acceptable agreement: in Fig. 14 we plot one-dimensional surface brightness profiles that we derive from our parameters and from the parameters of B95 as function of the major axis radius. As our data are not flux-calibrated we scale our models for the two components separately to match the B95 models at a radius of $40''$. We find that we have to adopt different zero points to match the two different components to the B95 data — they differ from each other by 0.7 mag. However, as the relative weights in the double-Gaussian decomposition are affected by differences in the relative line strengths in a non-trivial fashion, the zero points cannot be expected to be identical. Once the relative scaling has been established at one radius, the relative fluxes of our decomposition are very similar to those of the photometric decomposition.

[2] Following Ciotti (1991) we convert their r_e to a scale length by $h = r_e/1.678$.

We can therefore conclude with high confidence that the kinematic cold and hot stellar components of NGC 7217 found in this work are the photometric disk and spheroid components found by B95. This demonstrates that, given components that are sufficiently kinematically distinct, and a high enough spectral resolution, it is possible to spectrally decompose disk plus spheroid systems in a similar fashion to that common in photometric studies.

8.3 Stellar populations

In Section 5.3, we found evidence that the decoupling of the two stellar components is not only in their kinematics, but also in their chemical composition.

Differences in the chemical composition of kinematically decoupled stellar structures are observed in many classes of galaxies, and it is interpreted as the indication that the two stellar components have different origins. Observations range from large counter-rotating disks (Johnston et al. 2012; Coccato et al. 2011b; Johnston et al. 2012; Coccato et al. 2013), to counter-rotating bulges (Katkov et al. 2011), to small kinematically decoupled cores in early-type galaxies (e.g. Sil'chenko et al. 2002; Sil'Chenko 2005; McDermid et al. 2006)).

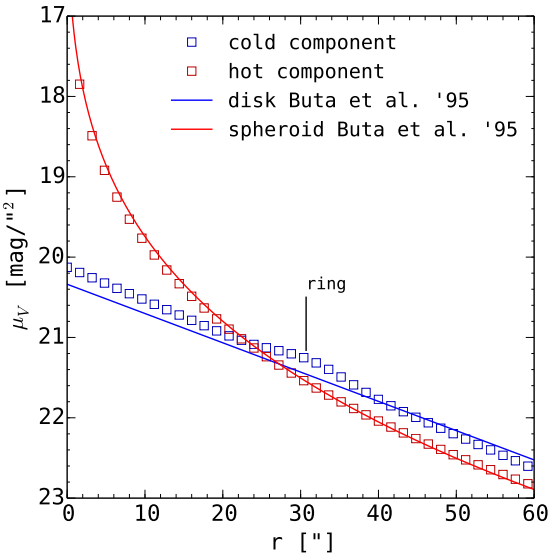

Figure 14. Surface brightness models for the total stellar content in NGC 7217. We fit two-dimensional models to the component images shown in Fig. 5 using the `Imfit` program by Peter Erwin. Similarly to B95, we model the hot component with a de Vaucouleurs' surface brightness distribution and the cold component with an exponential distribution. In the latter model we include a Gaussian ring. The open squares represent one-dimensional major-axis cuts through our models and the lines show the models derived by B95. As our data are not flux calibrated we chose a zero point to match our models against those of B95. We somewhat arbitrarily choose the zero points for an optimal fit at 40″. We note the need to apply zero points that differ by ≈0.7 mag to the two components.

For the particular case of NGC 7217, Jablonka, Martin & Arimoto (1996) measured Mg and Fe line strength indices, finding $Mg_2 = 0.28$ mag, Fe5270 = 3.04 Å, and Fe5335 = 2.45 Å. Sil'Chenko et al. (2011) performed a stellar template fit, and found age and metallicity gradients in the central 40″: the mean stellar age decreases from 10–13 Gyr in the centre to 5 Gyr while the metallicity decreases from nearly solar ([Fe/H] ≈ −0.06) to subsolar ([Fe/H] ≈ −0.3). Sarzi et al. (2007) found old ages (5–10 Gyr) in the central few arcseconds, consistent with Sil'Chenko et al. (2011), but extremely low metallicity ($Z = 0.05$ solar, i.e. [Fe/H] ≈ −1.3), inconsistent with the Silch'enko et al. values.

All these studies assumed a single stellar kinematic component when measuring the stellar population properties, and did not attempt to separate the kinematics. If we repeat the measurement on our spectra, considering only one kinematic stellar component, we measure a mean $\langle \mathrm{Fe} \rangle_{\mathrm{sing.\ comp.}} = 2.1 \pm 0.2$, which is slightly lower than that found by Jablonka, Martin & Arimoto (1996) ($\langle \mathrm{Fe} \rangle \approx 2.7$), and a mean $\mathrm{Mg}\,b_{\mathrm{sing.\ comp.}} = 2.9 \pm 0.2$.

We do not measure $H\beta$ so we cannot constrain the age with our measurements (see Section 4.4). However, if we adopt the age range 5 Gyr < Age < 10 Gyr found by Sil'Chenko et al. (2011) and Sarzi et al. (2007), we derive a metallicity range −0.3 < [Fe/H] < −0.2, consistent with the range obtained by Sil'Chenko et al. (2011), but not with that of Sarzi et al. (2007).

In Fig. 8 we compare the Lick indices for the two stellar components with (i) the typical values observed in the bulges of spiral galaxies given by Gorgas, Jablonka & Goudfrooij (2007, 32 galaxies) and Morelli et al. (2008, 15 galaxies)[3], and (ii) the typical values observed in early-type galaxies by Thomas et al. (2005, 124 galaxies). We note that the measurements for the hot stellar component, which we associate with the bulge component of the galaxy (Section 8.2), deviate from the mean values observed in the bulges of spiral galaxies. However, the central values of Mg b and $\langle$Fe$\rangle$ measured for the same component (top-right part of the measurement distributions in Fig. 8) are consistent with those measured in the central regions of early-type galaxies (Thomas et al. 2005).

8.4 Implications for the formation of NGC 7217

In the light of our findings it is interesting to revisit the question of the formation process of this particular galaxy. With its massive spheroid, it is likely that NGC 7217 experienced a major merger in its past, which may have been responsible for shutting down most of its star formation activity.

From SDSS images we derive a total extinction corrected $u - r$ color of 2.32 mag in a 9′ diameter aperture. This places NGC 7217 as a whole comfortably on the red sequence in a color magnitude diagram (Baldry, Bland-Hawthorn & Robertson 2004). If the relatively small contribution of the disk were to be removed, then the spheroid would appear even redder (B95). In fact, inside of the inner dust ring, where the spiral morphology disappears completely, $u - r = 2.7$ mag, placing NGC 7217 on the red flank of the red sequence. Compared to the correlations of effective radius, total stellar mass, luminosity, Sérsic index, and central velocity dispersion (Kormendy et al. 2009; Cappellari et al. 2013), the spheroid would also appear as a normal early-type galaxy.

The resemblance of the spheroidal component of NGC 7217 to an elliptical galaxy is further strengthened by the line index analysis. Indeed, the central values of the Mg b and $\langle$Fe$\rangle$ line strengths of the hot component are in good agreement with the values that Thomas et al. (2005) found in the central regions of early-type galaxies (see Fig. 8). We note the importance of the spectroscopic decomposition in measuring the line strengths of the disk and spheroid separately. In fact, the results of the single component analysis (Section 8.3) would place the bulge of NGC 7217 in the (Mg b,$\langle$Fe$\rangle$) plane closer to the bulges of spiral galaxies than to early-type galaxies (Fig. 8).

On the other hand, while its spheroid resembles in many respects a merger-built elliptical galaxy, NGC 7217 does host a stellar and a gaseous disk. However, the disk contains only about 20 % of the total light of the galaxy. Given its bluer

[3] We only consider the measurements from Gorgas, Jablonka & Goudfrooij (2007) obtained within half of the bulge effective radius. Measurements in Morelli et al. (2008) are performed in a region where the contribution to the total of the disk is equal or lower the contribution of the bulge, as indicated by their photometric bulge/disk decomposition.

colours it probably has a lower mass-to-light ratio than the spheroid, making the difference in stellar mass even more extreme. As such, NGC 7217 bears a resemblance to the Sombrero galaxy, which also looks in many respects like a typical elliptical galaxy if its thin, dusty disk is masked out. NGC 7217 may just be a nearly face-on version of Sombrero.

It is very unlikely that such a sub-dominant disk could have survived the merger itself; it must have reformed later on. Its bluer colours (B95), very low velocity dispersion and the sites of active star formation show that the stellar disk must be younger and is still in the process of growth. So what is the most likely formation scenario for the disk component in NGC 7217?

The disk may have formed as a consequence of a major merger. Such events can result in the formation of a cold disk if gas is already in place in the progenitors (Steinmetz & Navarro 2002; Barnes 2002; Abadi et al. 2003; Springel & Hernquist 2005; Robertson et al. 2006; Governato et al. 2007; Hopkins et al. 2009). For example, Governato et al. (2009) show that mergers can reform systems with bulge-to-disk ratios very close to the value that B95 found photometrically for NGC 7217.

Another possibility is that the gas that formed the disk was acquired later through minor mergers or cold accretion from the intergalactic medium (Mazzuca et al. 2006; Eliche-Moral et al. 2010). A factor seemingly pointing against accretion is the fact that NGC 7217 appears relatively isolated (Karachentseva 1973). This of course may not always have been the case but, the near-perfect alignment of the rotation axis of the spheroid and the gas disk strengthens that case against such a scenario. Misalignments between ionized gas and stellar kinematics do seem to be a common phenomenon; Davis et al. (2011) for instance finds misalignments in 42% of their field galaxies. In contrast, for NGC 7217 we find, with the exception of $r \leqslant 6''$, close to perfect alignment between the rotation axis of the ionized gas with the cold stellar component and the hot spheroidal component. If, however, the spheroid is not round but rotationally flattened, then it could force gas into alignment through gravitational torque. If we assume that the spheroid is axisymmetric, then the projected ellipticity of 0.08 (see Section 8.2) and an inclination of 33.9° (see Section 6), would correspond a substantial intrinsic flattening of 0.7. Correcting for the inclination, the maximum rotational velocity of the spheroid in the field of view of VIRUS-W is $90\,\mathrm{km\,s^{-1}}$. A dispersion of $170\,\mathrm{km\,s^{-1}}$ gives $v/\sigma = 0.8\sqrt{\varepsilon/(1-\varepsilon)}$, indicating that the flattening is close to the value expected for an isotropic rotator (Binney & Tremaine 1987; Kormendy 1982). Therefore, even if the spheroid is a perfectly isotropic system, its rotational flattening may have been sufficient to eradicate any prior misalignment between its own rotation axis and that of the gaseous disk.

It is possible that the gas is of internal origin, produced through, for example, stellar mass loss. Stellar mass loss may return as much as half of the stellar mass to the ISM over a Hubble time (Jungwiert, Combes & Palouš 2001; Lia, Portinari & Carraro 2002; Pozzetti et al. 2007; Parriott & Bregman 2008; Bregman & Parriott 2009). The formation of the disk in NGC 7127 would require that a reasonable fraction of the gas (≈20% for NGC 7217) can cool, recombine and reform a disk.

Fig. 8 contains some important clues on the origin of the disk. An obvious feature of that plot is the significant offset of the stellar populations of the hot spheroid and the cold disk. They form two completely separate sequences aligned roughly parallel to the one-to-one line of the (Mg b,⟨Fe⟩) plane. The sequences are separated from each other by at least 1 Å in either ⟨Fe⟩ strength or Mg b strength or both.

This is strikingly different to the cases of NGC 5719 Coccato et al. (2011a) or NGC 3593 and NGC 4550 (Coccato et al. 2013), where the two populations form essentially one continuous sequence. Taken by themselves, the spread in Mg b and ⟨Fe⟩ probably reflects the evolution of a single stellar population if it was left alone for a sufficient amount of time — gradually building up both α-elements and other metals over time. The location of a particular point along the sequence then reflects the different amounts of self-enrichment. The fact that both sequences show a very similar but modest increase of [α/Fe] towards the right of the plot indicates that in both cases the star formation was a prolonged process as a rapid burst would have caused a sudden change in [α/Fe].

Fig. 9 reveals that the spread of both sequences corresponds to negative radial Mg b and ⟨Fe⟩ gradients. If the above picture is correct, larger radii correspond to a lower degree of self-enrichment and probably lower ages, as would be expected in an inside-out growth scenario.

The cause of the offset of the two sequences may be understood in several ways: the analysis of the Mg b and Fe line strengths shows that the cold component has, on average, larger Fe and similar Mg to the hot component. This indicates that the disk must have experienced an extended star formation history, allowing for enrichment of the ISM by type Ia supernovae (e.g. Greggio & Renzini 1983; Thomas, Greggio & Bender 1998; Thomas et al. 2005). At first sight this extended star formation may have moved a disk population off the bulge sequence and gradually towards smaller [α/Fe](the upper left of Fig. 8). However, the fact that the disk never reaches larger metallicities than the spheroid seems to conflict with this scenario. Any prolonged star formation should also have enhanced the metallicity beyond that of the spheroid. The prolonged nature of this process makes it seem unlikely that it could cause the strong, observed bimodality.

Alternatively, through some event, the formation of the stars in the disk may have restarted at much lower metallicities than were present at the time in the spheroid. The disk population would then have developed starting at this lower metallicity towards the upper right hand of Fig. 9. An inflow of relatively primordial gas from some external reservoir would explain such a restart quite naturally. Gas that is available in the spheroid would be depleted, moving the sequence to the left of the plot. Any inflow of primordial material would at the same time leave [α/Fe] constant. The model lines of constant [α/Fe] then indicate that gas from the regions with the highest self-enrichment was depleted significantly and brought from $[Z/H] \approx 0.35$ down to values around −0.33 (following the 10 Gyr model lines). This would mean a factor of about five to one for depletion if the accreted material was truly primordial, and an even larger factor if it was partly pre-enriched. Given this, it seems most likely that the disk formation was triggered either through accretion from an external reservoir or through a minor merger event.

While our IFU data do not cover the whole area inside the effective radius, within the field of view the spheroid has a specific angular momentum of $\lambda_r = 0.17$ which would put it marginally into the regime of fast rotators (Emsellem et al. 2007). Sub-dominant disk structures are very common in early type galaxies (Bender et al. 1989; Rix & White 1990) and have been shown to exist in the majority of fast rotators (Krajnović et al. 2013). Aligned gas disks are also observed frequently in early-type galaxies (Davis et al. 2011). NGC 7217 seems to be one of the few cases found so far where the transformation of the gas disk into a stellar disk can actually be observed. With its total H I + H_2 mass of $\approx 1.2 \times 10^9 M_\odot$ and its relatively low level of star formation of $\approx 1\, M_\odot\, \mathrm{yr}^{-1}$ (B95), this process could be very long-lived. It may be that this is only possible because NGC 7217 happens to live in such relative isolation. It remains to be seen whether denser environments are able to shut off star formation in these low disk-to-total systems as they do in large-scale disks (Koopmann & Kenney 2004).

One more definite conclusion can be drawn from our findings concerning the origin of the ring structure: Verdes-Montenegro, Bosma & Athanassoula (1995) conducted a detailed analysis of the ring structure and concluded that the ring locations can be identified with the outer and inner Lindblad resonance and the 4:1 ultra-harmonic resonance of a distortion in the axisymmetry. But NGC 7217 lacks obvious distortions such as a bar, an oval or a strong spiral structure. We can now exclude the possibility that instabilities caused by stellar counter-rotation (Lovelace, Jore & Haynes 1997) are responsible for the formation of the ring structure in NGC 7217. The counter-rotation has also been attributed to a previous minor merger (Comerón et al. 2010; Grouchy et al. 2010), which could have led to the ring structure. Based on our findings, the scenario proposed by B95 now seems most likely: a weak non-axisymmetric distortion, discovered only through a careful Fourier analysis, generates the resonance that results in the rings.

9 CONCLUSIONS

Using the novel VIRUS-W spectrograph we have obtained moderately high resolution $R \approx 9000$ optical Integral Field Unit observations of NGC 7217. Based on our high signal-to-noise data we are able to revisit the kinematic structure of this galaxy and to test previous claims of the existence of a counter-rotating stellar disk. Using a new algorithm, we derive non-parametrized line-of-sight velocity distributions and carry out double-Gaussian decompositions. We also use the methodology introduced by Coccato et al. (2011b, 2013) to confirm our findings and to derive line strength indices for the two stellar components.

Our main findings are:

- We confirm the existence of two dynamically distinct stellar components. In contrast to previous claims by Merrifield & Kuijken (1994), Sil'chenko & Afanasiev (2000), and Fabricius et al. (2012b) we do not find them to be counter rotating. Rather we are able to decompose them into one hot, dominant, round, slowly-rotating component with a velocity dispersion of $\approx 170\,\mathrm{km\,s^{-1}}$, and a cold, co-rotating stellar disk with a velocity dispersion of $\approx 20\,\mathrm{km\,s^{-1}}$.
- The velocity and velocity dispersion fields of the cold stellar disk are very similar to those of the gas as derived from the [O III] emission lines. Together with the blue colours of the rings in this galaxy (B95) and the visible sites of active star formation, this supports a picture where the stellar disk is still in the process of regrowing.
- The kinematic position angles of the cold stellar disk component and the hot spheroidal component are identical within our measurement errors, rendering an external origin of the gas unlikely.
- We find an increase of velocity dispersion of the gas at the inner stellar ring. This may be a result of the resonant nature of the ring, but also a result of the ongoing star formation in that region.
- The two components are clearly separated in (Mg b,⟨Fe⟩) space in the sense that the disk component shows larger equivalent widths in ⟨Fe⟩ and lower equivalent widths in Mg b that cannot be explained by an age difference. This points to a different star formation history, with a shorter-lived period of star formation in the spheroid and a later and/or longer-lived star formation in the disk.
- The Lick indices measured in the central regions of the hot component are more similar to those in the central regions of elliptical galaxies than to those in the bulges of spirals.
- We confirm the existence of a misalignment of the gas velocity field in the central arcseconds. We attempt a tilted ring model, but cannot confirm a 90° angular separation between the central disk and the outer disk rotation axes as would be necessary for a polar ring that was described by Zasov & Sil'chenko (1997); Sil'chenko & Afanasiev (2000). The maximum angular separation we find is 30°. While this may be a consequence of the limited spatial resolution of our data, we stress that a natural explanation for the central deviation from the global rotation could lie in the weak break in axisymmetry that was reported by B95 (Athanassoula 1992).
- The tilted ring analysis provides a rotation curve for the gas. This allows us to derive the total enclosed dynamical mass and a deprojected mass-to-light ratio of $\Upsilon^*_{dyn} = 4.5 M_\odot/L_\odot$. Using GALXEX FUV/NUV, SDSS, and IRAC I1,2,3 bands we also conduct a stellar population analysis inside the central 10″ and find that the predicted mass-to-light ratio is in reasonable agreement with the dynamical value if a Kroupa IMF is assumed.
- The structural parameters of the two stellar components (scale lengths, ellipticities and position angles) are in good agreement with the values obtained from photometry (B95). This demonstrates that a kinematic decomposition is feasible for spheroid/disk systems. This method has the advantage of being completely model free; it does not rely on the extrapolation of model profiles. As such, it is fully complementary to photometric methods and allows us to test, for instance, assumptions where all the light that exceeds the inwards extrapolation of an outer exponential disk is attributed to the bulge of a system. It also enables us to probe the kinematic properties and to measure stellar population parameters beyond broadband colours. This extends the technique of the spectral decomposition (Coccato et al. 2011b, 2013) from the application to counter-rotating stellar disks to spheroid-disk systems, as long as the two components have sufficient separation in velocity dispersion. This

makes it possible to probe the origins of individual components in a multicomponent system separately and unambiguously, rendering it a powerful tool to study the formation of such galaxies.

We suggest that the main bulk of stars in NGC 7217, i.e. the spheroidal component, formed through a major merger. The merger remnant has photometric and spectroscopic properties more similar to those of an elliptical galaxy than to those of the bulges of spiral galaxies. The disk component formed after the merger, presumably from relatively primordial gas acquired through minor mergers or cold accretion from the intergalactic medium (Mazzuca et al. 2006; Eliche-Moral et al. 2010), or an external reservoir as suggested by the significant offset of the two stellar populations in the (Mg b,$\langle$Fe$\rangle$) plane.

ACKNOWLEDGEMENTS

L.C. acknowledges financial support from the European Communitys Seventh Framework Program (/FP7/2007-2013/) under grant agreement No. 229517. We would like to thank Dave Wilman for fruitful discussions on the implications of a disk regrowth scenario. We wish to thank Peter Erwin for making his `Imfit` code available to us. We wish to thank Eric Emsellem for making the Python version of the Voronoi binning code available to us. This research made use of APLpy, an open-source plotting package for Python hosted at http://aplpy.github.com. This research has made use of the NASA/IPAC Extragalactic Database (NED) which is operated by the Jet Propulsion Laboratory, California Institute of Technology, under contract with the National Aeronautics and Space Administration. Some of the data presented in this paper were obtained from the Mikulski Archive for Space Telescopes (MAST). STScI is operated by the Association of Universities for Research in Astronomy, Inc., under NASA contract NAS5-26555. Support for MAST for non-HST data is provided by the NASA Office of Space Science via grant NNX13AC07G and by other grants and contracts. This work is based in part on archival data obtained with the Spitzer Space Telescope, which is operated by the Jet Propulsion Laboratory, California Institute of Technology under a contract with NASA. Support for this work was provided by an award issued by JPL/Caltech. Funding for the SDSS and SDSS-II has been provided by the Alfred P. Sloan Foundation, the Participating Institutions, the National Science Foundation, the U.S. Department of Energy, the National Aeronautics and Space Administration, the Japanese Monbukagakusho, the Max Planck Society, and the Higher Education Funding Council for England. The SDSS Web Site is http://www.sdss.org/. The SDSS is managed by the Astrophysical Research Consortium for the Participating Institutions. The Participating Institutions are the American Museum of Natural History, Astrophysical Institute Potsdam, University of Basel, University of Cambridge, Case Western Reserve University, University of Chicago, Drexel University, Fermilab, the Institute for Advanced Study, the Japan Participation Group, Johns Hopkins University, the Joint Institute for Nuclear Astrophysics, the Kavli Institute for Particle Astrophysics and Cosmology, the Korean Scientist Group, the Chinese Academy of Sciences (LAMOST), Los Alamos National Laboratory, the Max-Planck-Institute for Astronomy (MPIA), the Max-Planck-Institute for Astrophysics (MPA), New Mexico State University, Ohio State University, University of Pittsburgh, University of Portsmouth, Princeton University, the United States Naval Observatory, and the University of Washington.

APPENDIX A: ON THE CHOICE OF REGULARISATION FOR THE KINEMATIC EXTRACTION

The Maximum Penalized Likelihood method for the derivation of non-parametric LOSVDs introduces the smoothing parameter as described in Section 4.2. It penalizes the sum of the squared second derivative of the LOSVD. If the smoothing factor is set to zero no penalization occurs and the derived LOSVDs tend to show strong noise-induced fluctuations. Non-zero smoothing factors dampen the fluctuations at the cost of the potential introduction of biases. Similar regularisation schemes are also part of other algorithms for the derivation of LOSVDs such as pPXF (Cappellari & Emsellem 2004) and the actual degree of penalization is typically chosen through Monte Carlo simulations: a sample of synthetic spectra with artificial noise according to specific signal-to-noise value is generated. The degree of regularisation is then chosen such that it does not bias the moments of the derived LOSVDs significantly (e.g. Nowak et al. 2008).

In this work we specifically wish to study the shape of the full LOSVD. We therefore cannot base our choice on the moments of the LOSVD. We decide instead to use a smoothing factor that is small enough that it results in a non-significant increase of the RMS value of the residuals between the recorded spectra and the preferred broadened model. This very conservative approach results in LOSVDs which still show a fair degree of oscillations (see Fig. 3). These oscillations have amplitudes that are generally compatible with the statistical error in each of the velocity channels. They are due to the fact that the smoothing acts on a typical velocity scale, the size of which is controlled by the smoothing factor: the penalization of the second derivative necessarily introduces a correlation between neighbouring channels. Any noise spike will pull up the channels next to it. An increase of the smoothing will act over larger velocity separations and therefore increase the velocity scale that the oscillations occur on.

The effect of different degrees of regularisation is shown for the example of a single bin in Fig. A1. The upper four curves show the LOSVDs that we derive from the spectrum of bin 130. With stronger smoothing, oscillations occur on increasingly longer scales until they are completely dampened out by a smoothing of 5000. The genuine narrow dispersion component at about -150 $\mathrm{km\,s^{-1}}$ does not disappear, but it does get significantly broadened. The underlying broad component remains nearly unaffected. The bottom-most distribution in Fig. A1 was derived for a simulated spectrum that was created by broadening a template spectrum with a two-component Gaussian kernel with the same parameters that we derived for bin 130. The level of noise-induced oscillations is very similar to the one seen in the LOSVDs that we derived with the same smoothing from

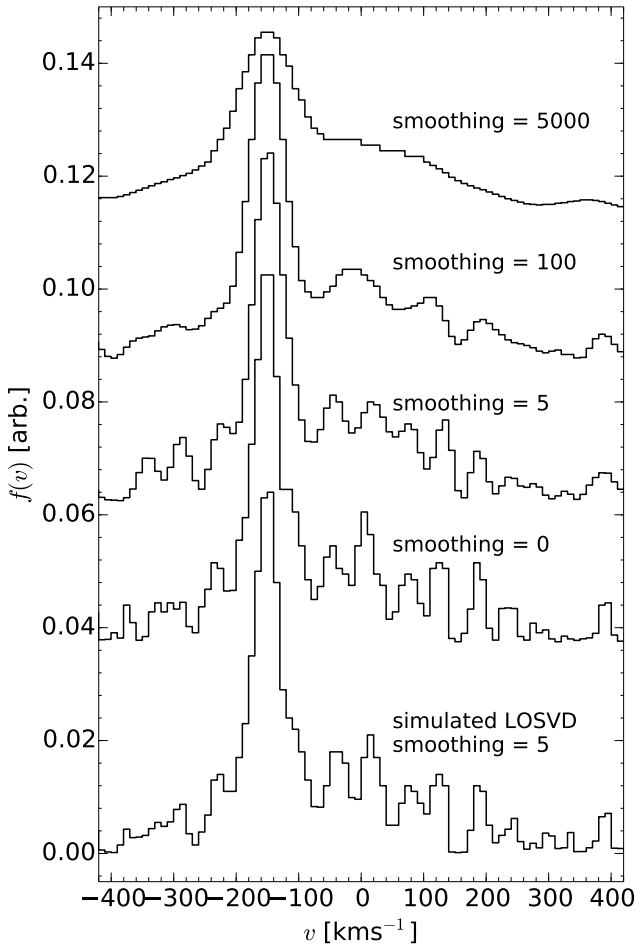

Figure A1. The best-fitting non-parametric LOSVDs for different choices of the smoothing value. All but the bottom-most curves represent LOSVDs derived from the actual spectrum of bin 130, as shown in the upper panel of Fig. 3. Stronger penalization of the second derivative results in smoother LOSVDs at the cost of artificially broadening the narrow dispersion component at -150 $\mathrm{km\,s^{-1}}$. The bottom-most distribution was derived from a simulated spectrum that was broadened with a double-Gaussian kernel with the same parameters that we derive in the decomposition for bin 130.

the actual data. In the case of a single component LOSVD that is well-approximated by a single Gaussian distribution, the smoothing can be set large enough that over that scale of the LOSVD any oscillations are dampened out. For the case of the two component LOSVDs of NGC 7217 this is not possible, but the choice of our small smoothing values guarantees that our derived dispersions are not biased toward large values.

REFERENCES

Abadi M. G., Navarro J. F., Steinmetz M., Eke V. R., 2003, ApJ, 591, 499
Adams J. J. et al., 2011, ApJs, 192, 5
Anderson E., Francis C., 2012, Astronomy Letters, 38, 331
Árnadóttir A. S., Feltzing S., Lundström I., 2010, A&A, 521, A40
Athanassoula E., 1992, MNRAS, 259, 345
Baldry I. K., Bland-Hawthorn J., Robertson J. G., 2004, PASP, 116, 403
Barnes J. E., 2002, MNRAS, 333, 481
Bender R., 1988, A&A, 202, L5
Bender R., 1990, A&A, 229, 441
Bender R., Surma P., Doebereiner S., Moellenhoff C., Madejsky R., 1989, A&A, 217, 35
Bertola F., Cinzano P., Corsini E. M., Pizzella A., Persic M., Salucci P., 1996, ApJ, 458, L67+
Binney J., Merrifield M., 1998, Galactic Astronomy
Binney J., Tremaine S., 1987, Galactic dynamics
Bregman J. N., Parriott J. R., 2009, ApJ, 699, 923
Bruzual G., Charlot S., 2003, MNRAS, 344, 1000
Buta R., van Driel W., Braine J., Combes F., Wakamatsu K., Sofue Y., Tomita A., 1995, ApJ, 450, 593
Cappellari M., Copin Y., 2003, MNRAS, 342, 345
Cappellari M., Emsellem E., 2004, PASP, 116, 138
Cappellari M. et al., 2013, MNRAS, 432, 1862
Ciotti L., 1991, A&A, 249, 99
Coccato L., Corsini E. M., Pizzella A., Bertola F., 2007, A&A, 465, 777
Coccato L., Gerhard O., Arnaboldi M., Ventimiglia G., 2011a, A&A, 533, A138
Coccato L., Morelli L., Corsini E. M., Buson L., Pizzella A., Vergani D., Bertola F., 2011b, MNRAS, 412, L113
Coccato L., Morelli L., Pizzella A., Corsini E. M., Buson L. M., Dalla Bontà E., 2013, A&A, 549, A3
Comerón S., Knapen J. H., Beckman J. E., Laurikainen E., Salo H., Martínez-Valpuesta I., Buta R. J., 2010, MNRAS, 402, 2462
Davies R. L., Birkinshaw M., 1988, ApJs, 68, 409
Davis T. A. et al., 2011, MNRAS, 417, 882
de Vaucouleurs G., 1959, Handbuch der Physik, 53, 275
de Zeeuw T., Franx M., 1989, ApJ, 343, 617
Eliche-Moral M. C., González-García A. C., Balcells M., Aguerri J. A. L., Gallego J., Zamorano J., 2010, in American Institute of Physics Conference Series, Vol. 1240, American Institute of Physics Conference Series, Debattista V. P., Popescu C. C., eds., pp. 237–238
Emsellem E. et al., 2007, MNRAS, 379, 401
Emsellem E. et al., 2004, MNRAS, 352, 721
Erwin P., 2014, in prep.
Fabricius M. H., Barnes S., Bender R., Drory N., Grupp F., Hill G. J., Hopp U., MacQueen P. J., 2008, in Society of Photo-Optical Instrumentation Engineers (SPIE) Conference Series, Vol. 7014, Society of Photo-Optical Instrumentation Engineers (SPIE) Conference Series
Fabricius M. H. et al., 2012a, in Society of Photo-Optical Instrumentation Engineers (SPIE) Conference Series, Vol. 8446, Society of Photo-Optical Instrumentation Engineers (SPIE) Conference Series
Fabricius M. H., Saglia R. P., Fisher D. B., Drory N., Bender R., Hopp U., 2012b, ApJ, 754, 67
Fisher D. B., Drory N., 2008, AJ, 136, 773
Fisher D. B., Drory N., 2010, ApJ, 716, 942
Franx M., Illingworth G. D., 1988, ApJ, 327, L55

Gebhardt K. et al., 2000, AJ, 119, 1157
Gerhard O. E., 1993, MNRAS, 265, 213
Gil de Paz A. et al., 2007, ApJs, 173, 185
Gorgas J., Jablonka P., Goudfrooij P., 2007, A&A, 474, 1081
Gössl C., Bender R., Fabricius M., Hopp U., Karasz A., Kosyra R., Lang-Bardl F., 2012, in Society of Photo-Optical Instrumentation Engineers (SPIE) Conference Series, Vol. 8446, Society of Photo-Optical Instrumentation Engineers (SPIE) Conference Series
Gössl C. A., Riffeser A., 2002, A&A, 381, 1095
Governato F. et al., 2009, MNRAS, 398, 312
Governato F., Willman B., Mayer L., Brooks A., Stinson G., Valenzuela O., Wadsley J., Quinn T., 2007, MNRAS, 374, 1479
Greggio L., Renzini A., 1983, A&A, 118, 217
Grouchy R. D., Buta R. J., Salo H., Laurikainen E., 2010, AJ, 139, 2465
Haynes M. P., Jore K. P., Barrett E. A., Broeils A. H., Murray B. M., 2000, AJ, 120, 703
Hill G. J., Gebhardt K., Komatsu E., MacQueen P. J., 2004, in American Institute of Physics Conference Series, Vol. 743, The New Cosmology: Conference on Strings and Cosmology, R. E. Allen, D. V. Nanopoulos, & C. N. Pope, ed., pp. 224–233
Hill G. J. et al., 2010, in Society of Photo-Optical Instrumentation Engineers (SPIE) Conference Series, Vol. 7735, Society of Photo-Optical Instrumentation Engineers (SPIE) Conference Series
Hill G. J. et al., 2008, in Society of Photo-Optical Instrumentation Engineers (SPIE) Conference Series, Vol. 7014, Society of Photo-Optical Instrumentation Engineers (SPIE) Conference Series
Hopkins P. F., Cox T. J., Younger J. D., Hernquist L., 2009, ApJ, 691, 1168
Hopp U. et al., 2012, in Society of Photo-Optical Instrumentation Engineers (SPIE) Conference Series, Vol. 8444, Society of Photo-Optical Instrumentation Engineers (SPIE) Conference Series
Jablonka P., Martin P., Arimoto N., 1996, AJ, 112, 1415
Jedrzejewski R., Schechter P. L., 1989, AJ, 98, 147
Johnston E. J., Aragón-Salamanca A., Merrifield M. R., Bedregal A. G., 2012, MNRAS, 422, 2590
Jore K. P., Broeils A. H., Haynes M. P., 1996, AJ, 112, 438
Jungwiert B., Combes F., Palouš J., 2001, A&A, 376, 85
Karachentseva V. E., 1973, Astrofizicheskie Issledovaniia Izvestiya Spetsial'noj Astrofizicheskoj Observatorii, 8, 3
Katkov I., Chilingarian I., Sil'chenko O., Zasov A., Afanasiev V., 2011, Baltic Astronomy, 20, 453
Katkov I. Y., Sil'chenko O. K., Afanasiev V. L., 2013, ApJ, 769, 105
Koleva M., Vazdekis A., 2012, A&A, 538, A143
Koopmann R. A., Kenney J. D. P., 2004, ApJ, 613, 851
Kormendy J., 1982, in Saas-Fee Advanced Course 12: Morphology and Dynamics of Galaxies, L. Martinet & M. Mayor, ed., pp. 113–288
Kormendy J., Fisher D. B., Cornell M. E., Bender R., 2009, ApJs, 182, 216
Krajnović D. et al., 2013, MNRAS, 432, 1768
Krajnović D., Cappellari M., de Zeeuw P. T., Copin Y., 2006, MNRAS, 366, 787
Krajnović D. et al., 2011, MNRAS, 414, 2923
Kroupa P., 2001, MNRAS, 322, 231
Kuijken K., Fisher D., Merrifield M. R., 1996, MNRAS, 283, 543
Lia C., Portinari L., Carraro G., 2002, MNRAS, 330, 821
Lovelace R. V. E., Jore K. P., Haynes M. P., 1997, ApJ, 475, 83
Magorrian J., 1999, MNRAS, 302, 530
Martin D. C. et al., 2005, ApJ, 619, L1
Mazzuca L. M., Sarzi M., Knapen J. H., Veilleux S., Swaters R., 2006, ApJ, 649, L79
McDermid R. M. et al., 2006, MNRAS, 373, 906
Merrifield M. R., Kuijken K., 1994, ApJ, 432, 575
Moré J. J., Garbow B. S., Hillstrom K. E., 1980, User guide for minpack-1
Morelli L. et al., 2008, MNRAS, 389, 341
Nowak N., Saglia R. P., Thomas J., Bender R., Davies R. I., Gebhardt K., 2008, MNRAS, 391, 1629
Parriott J. R., Bregman J. N., 2008, ApJ, 681, 1215
Pizzella A., Corsini E. M., Vega Beltrán J. C., Bertola F., 2004, A&A, 424, 447
Pozzetti L. et al., 2007, A&A, 474, 443
Prada F., Gutierrez C. M., Peletier R. F., McKeith C. D., 1996, ApJ, 463, L9+
Prugniel P., Soubiran C., 2001, A&A, 369, 1048
Rix H.-W., Franx M., Fisher D., Illingworth G., 1992, ApJ, 400, L5
Rix H.-W., White S. D. M., 1990, ApJ, 362, 52
Robertson B., Bullock J. S., Cox T. J., Di Matteo T., Hernquist L., Springel V., Yoshida N., 2006, ApJ, 645, 986
Rubin V. C., Graham J. A., Kenney J. D. P., 1992, ApJ, 394, L9
Russell D. G., 2002, ApJ, 565, 681
Saglia R. P. et al., 2010, A&A, 509, A61+
Salpeter E. E., 1955, ApJ, 121, 161
Sánchez-Blázquez P. et al., 2006, MNRAS, 371, 703
Sarzi M., Allard E. L., Knapen J. H., Mazzuca L. M., 2007, MNRAS, 380, 949
Sarzi M. et al., 2006, MNRAS, 366, 1151
Schlafly E. F., Finkbeiner D. P., 2011, ApJ, 737, 103
Schlegel D. J., Finkbeiner D. P., Davis M., 1998, ApJ, 500, 525
Scorza C., Bender R., 1990, A&A, 235, 49
Scorza C., Bender R., 1995, A&A, 293, 20
Sil'Chenko O. K., 2005, Astronomy Letters, 31, 227
Sil'chenko O. K., Afanasiev V. L., 2000, A&A, 364, 479
Sil'chenko O. K., Afanasiev V. L., Chavushyan V. H., Valdes J. R., 2002, ApJ, 577, 668
Sil'Chenko O. K., Chilingarian I. V., Sotnikova N. Y., Afanasiev V. L., 2011, MNRAS, 414, 3645
Sil'chenko O. K., Moiseev A. V., 2006, AJ, 131, 1336
Springel V., Hernquist L., 2005, ApJ, 622, L9
Steinmetz M., Navarro J. F., 2002, NewA, 7, 155
Thomas D., Greggio L., Bender R., 1998, MNRAS, 296, 119
Thomas D., Maraston C., Bender R., 2003a, MNRAS, 343, 279
Thomas D., Maraston C., Bender R., 2003b, MNRAS, 339, 897
Thomas D., Maraston C., Bender R., Mendes de Oliveira C., 2005, ApJ, 621, 673
Thomas J. et al., 2011, MNRAS, 415, 545

Treu T., Auger M. W., Koopmans L. V. E., Gavazzi R., Marshall P. J., Bolton A. S., 2010, ApJ, 709, 1195
Verdes-Montenegro L., Bosma A., Athanassoula E., 1995, A&A, 300, 65
Vergani D., Pizzella A., Corsini E. M., van Driel W., Buson L. M., Dettmar R.-J., Bertola F., 2007, A&A, 463, 883
Werner M. W. et al., 2004, ApJs, 154, 1
Worthey G., Faber S. M., Gonzalez J. J., Burstein D., 1994, ApJs, 94, 687
Worthey G., Ottaviani D. L., 1997, ApJs, 111, 377
York D. G. et al., 2000, AJ, 120, 1579
Zasov A. V., Sil'chenko O. K., 1997, Astronomy Reports, 41, 734
Zeilinger W. W., Vega Beltrán J. C., Rozas M., Beckman J. E., Pizzella A., Corsini E. M., Bertola F., 2001, APSS, 276, 643